

Submillimeter observations of molecular gas interacting with the supernova remnant W28

Parichay Mazumdar¹, Le Ngoc Tram¹, Friedrich Wyrowski¹, Karl M. Menten¹, and Xindi Tang^{1,2,3}

¹ Max-Planck-Institut für Radioastronomie, Auf dem Hügel 69, 53121 Bonn, Germany
e-mail: pmazumdar@mpifr-bonn.mpg.de

² Xinjiang Astronomical Observatory, Chinese Academy of Sciences, 830011 Urumqi, PR China

³ Key Laboratory of Radio Astronomy, Chinese Academy of Sciences, 830011 Urumqi, PR China

Received xxx / Accepted xxx

ABSTRACT

Context. Supernovae (SNe) inject large amounts of energy and chemically enriched materials into their surrounding interstellar medium and, in some instances, into molecular clouds (MCs). The interaction of a supernova remnant (SNR) with a MC plays a crucial role in the evolution of the cloud's physical and chemical properties. Despite their importance, only a handful of studies have been made addressing the molecular richness in molecular clouds impacted by SNRs. (Sub)millimeter wavelength observations of MCs affected by SNRs can be used to build a census of their molecular richness, which in turn can motivate various chemical and physical models aimed at explaining the chemical evolution of the clouds.

Aims. We carried out multi-molecule and multi-transition observations toward the molecular region F abutting the SNR W28, containing 1720 MHz OH masers, well-established tracers of SNR-MC interactions. We used the detected lines to constrain the physical conditions of this region.

Methods. We used the APEX Telescope to observe molecular lines in the frequency range 213–374 GHz. We used non-local thermodynamic equilibrium (non-LTE) RADEX modeling to interpret the observational data.

Results. We detected emission from multiple molecular species in the region, namely CH₃OH, H₂CO, SO, SiO, CN, CCH, NO, CS, HCO⁺, HCN, HNC, N₂H⁺, CO, and from the isotopologues of some of them. We report the first detection of thermally excited (non-maser) CH₃OH emission toward a SNR. Employing non-LTE RADEX modeling of multiple H₂CO and CH₃OH lines, we constrained the kinetic temperature and spatial density in the molecular gas. The gas kinetic temperatures range from 60 to 100 K while the spatial density of the gas ranges from 9×10^5 to 5×10^6 cm⁻³. We obtained an ortho-para ratio ~ 2 for H₂CO, which indicates that formaldehyde is most likely formed on dust grain surfaces and not in the gas phase.

Conclusions. Our results show that molecules as complex as H₂CO and CH₃OH can be detected in SNR-MC interactions. This could motivate chemical modeling to explore their formation pathways.

Key words. ISM: supernova remnants – ISM: molecules – astrochemistry – line: profiles – molecular processes – radiative transfer – shock waves – ISM: individual objects – ISM: abundances – ISM: clouds – ISM: kinematics and dynamics – Submillimeter: ISM

1. Introduction

Supernovae (SNe) are highly energetic phenomena injecting large amounts of energy ($\sim 10^{51}$ erg) and momentum, along with chemically enriched material into the interstellar medium (ISM) (Dubner & Giacani 2015). They are considered to be a major source of interstellar turbulence and galactic outflows (Li et al. 2017, and references therein). Their expanding leftovers, referred to as supernova remnants (SNRs), may interact with the ambient or even the parent molecular clouds (MCs) of their massive stellar precursors. This interaction compresses the gas and converts the kinetic energy to thermal energy; thus the gas is heated through the shock passage and the ram pressure of the parent MC is enhanced (Chevalier 1999). All of this triggers chemical reactions which are otherwise unlikely or even impossible in MCs thereby boosting the abundance of molecular species that are usually rare in quiescent gas (Tielens 2005). One example of this is the detection of SiO emission from SNR W51C (Dumas et al. 2014), a well-established molecular tracer of shocks (Schilke et al. 1997).

SNR-MC interactions have been intensively studied by observations of the shocked regions by using both molecular and

atomic gas tracers (see e.g., Wootten 1977; Denoyer 1979a,b; Wootten 1981; Denoyer 1983; Tatematsu et al. 1985, 1987; Fukui & Tatematsu 1988; Tatematsu et al. 1990a,b; White et al. 1987; van Dishoeck et al. 1993; White 1994; Koo & Moon 1997a,b; Seta et al. 1998, 2004; Wilner et al. 1998; Arikawa et al. 1999; Reach & Rho 1999, 2000; Reach et al. 2002, 2005a; Neufeld et al. 2007; Yuan & Neufeld 2011; Gusdorf et al. 2012; Anderl et al. 2014; Reach et al. 2019; Dell'Ova et al. 2020; Rho et al. 2021). Commonly, the rovibrational lines of H₂ and CO are notably used to characterize the SNR shocks. With no permanent dipole moment, H₂ is excited at high levels of excitation energy, which is optimally probed in early regions in shock. Owing to a dipole moment, CO complements H₂ by probing the cooler and denser part in the shocked regions. Both the excitation diagram ("Boltzmann plot"), relation between the column density of the rotationally excited levels and their energy above the ground state, e.g., Neufeld et al. 2007; Yuan & Neufeld 2011), and the resolved velocity profiles (e.g., Reach et al. 2019; Rho et al. 2021) have been used to constrain the physical properties of the shocked gas.

(Sub)millimeter and mm observations of SNRs can be used to build a census of their molecular richness, which, in turn, can

help in constraining various chemical and physical models aimed at explaining the evolution of MCs interacting with SNRs. These observations also provide input for shocked molecular cloud astrochemistry in general. In one of the few existing studies exploring the molecular richness in an MC-SNR interaction region, [van Dishoeck et al. \(1993\)](#) carried out a molecular search in the shocked gas region of the SNR IC 443 and found high frequency lines of HCO^+ , HCN, HNC, CS, SO, SiO, H_2CO , and C_2H . Until today this has been the only extensive study of the inventory of molecular richness existing in SNR-MC interaction regions.

For a long time, maser emission in the 1720 MHz satellite hyperfine structure transition of the hydroxyl radical (OH) has served as a unique molecular signpost of SNR-MC interactions. Even though this line is detected relatively rarely (i.e., in $\sim 10\%$ SNR, [Green et al. 1997](#)) it can be used for probing the non-dissociative C-type shock and it provides a direct estimate of the magnetic field strength via the Zeeman effect ([Lockett et al. 1999](#)).

In this work, we report observations with the APEX telescope of emission lines from various molecular species toward region F of the SNR W28, which is a known source of 1720 MHz OH emission (see Figure 1). Our work, thus, fills a gap between (sub)mm studies and FIR/MIR/NIR and radio line studies of SNR-MC interactions.

W28 is a composite-type SNR that appears as a shell that is 42' in diameter in the radio continuum emission ([Green 1998](#); [Dubner et al. 2000](#)) and is located at $l=6.4^\circ$, $b=-0.2^\circ$ in the Galactic plane (see Fig. 1). It shows thermal X-Ray emission ([Rho & Borkowski 2002](#)) as well as gamma ray sources ([Aharonian et al. 2008](#); [Giuliani et al. 2010](#); [Abdo et al. 2010](#)). Many CO studies ([Arikawa et al. 1999](#); [Reach et al. 2005b](#); [Fukui 2008](#)) show massive molecular clouds toward the north-east and the south of the SNR. Emission lines from these clouds were found to be mostly centered at a local standard of rest velocity, V_{LSR} , of $\approx 7 \text{ km s}^{-1}$, which is consistent with values estimated from HI observations ([Velázquez et al. 2002](#)). The interaction of the SNR shock with the molecular cloud towards its east side appears to be responsible for the enhanced synchrotron and thermal X-ray emissions ([Dubner et al. 2000](#)). Broad CO line widths ($\Delta V = 30\text{--}50 \text{ km s}^{-1}$) were observed by [Frail & Mitchell \(1998\)](#) along the gaseous ridges of the molecular cloud facing the shock front while the lines off the ridges were narrow. A very high energy (VHE) γ -ray emission source, HESS J1801-233 ([Aharonian et al. 2008](#)), is also coincident with the northeastern boundary of W28, providing further evidence of SNR-MC interactions. Multiple regions of 1720 MHz OH maser emissions (with V_{LSR} ranging between 5 and 15 km s^{-1}), loosely distributed in six areas (A–F) ([Claussen et al. 1997](#)) were also found towards the north eastern regions of W28 (see Fig. 1). These masers were found to be preferentially located along the interface between the shock and the interacting molecular cloud, supporting the hypothesis that they were excited due to the interaction between the two ([Frail & Mitchell 1998](#); [Dubner et al. 2000](#)). The APEX observations discussed in the present paper were carried out towards the F group of OH masers shown in Fig. 2.

This paper is structured as follows. We describe the observations and data reduction procedure in Sect. 2. Our data analysis and results are described in Sect. 3. In Sect. 4, we derive the physical properties using the non-LTE RADEX code. Our discussion and conclusion are given in Sects. 5 and 6.

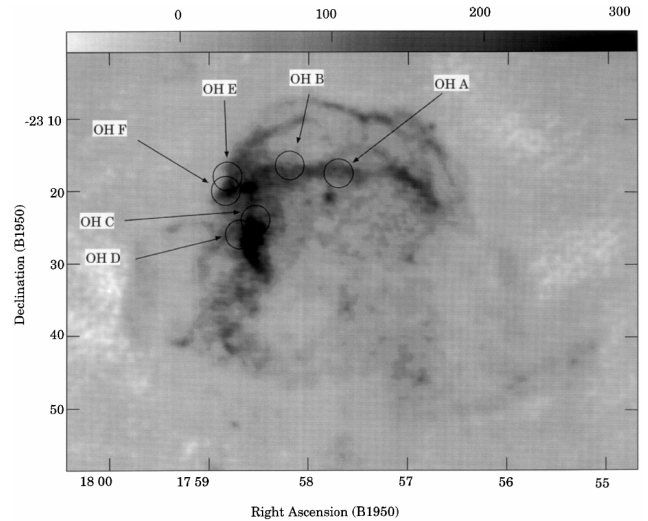


Fig. 1. 327 MHz radio continuum image ([Frail et al. 1993](#)) of the W28 SNR borrowed from Figure 1 of [Claussen et al. \(1997\)](#). The gray scale at the top is in units of mJy beam^{-1} . The location of the OH (1720 MHz) emission concentrations have been marked with black circles. The sub-mm wavelength observations reported here were carried out towards the F group of OH masers shown in Fig. 2.

2. Observations and data reduction

2.1. Observations

The data were taken with the 12 m single dish Atacama Pathfinder EXperiment (APEX) submillimeter telescope on Llano Chajnantor, Chile over multiple observing sessions between 2011 August and 2012 July under the project number M-087.F-0041-2011¹. The heterodyne SIS receivers APEX-1 (213–275 GHz) and FLASH (268–374 GHz) were used. With FLASH it was possible to observe both side bands simultaneously, while APEX-1 could only observe one side band at a time. System temperatures were in the range 150–400 K. Table 1 shows a summary of the frequency settings used during the observations. Two extended-bandwidth fast Fourier transform spectrometers (XFFTSs) were used as backends. With an instantaneous bandwidth of 2.5 GHz, 32768 channels, and a 1 GHz overlap, the backends covered the entire 4 GHz (lower and upper sideband) intermediate-frequency (IF) range of the receivers. This roughly translates to a velocity resolution of 0.094 and 0.072 km s^{-1} at 245 and 320 GHz, respectively.

Guided by the positions of the OH masers in region F, at the beginning of the first observing run, a raster map was observed to find the position of strongest methanol emission in the molecular F region. Figure 2 shows an integrated intensity map of the CH_3OH ($J = 6_0 - 5_0 \text{ A}^+$) transition on a 5×5 grid (measured with a $10''$ spacing) centered at an offset of $(10'', -30'')$ from the center of the CO $J = 3-2$ map of the W28 F region presented by [Frail & Mitchell \(1998\)](#), which is at $(\alpha, \delta)_{\text{J2000}} = 18^{\text{h}}01^{\text{m}}51^{\text{s}}8, -23^{\circ}18'59''$. The methanol peak thus is located at $(\alpha, \delta)_{\text{J2000}} = 18^{\text{h}}01^{\text{m}}52^{\text{s}}5, -23^{\circ}19'29''$. All subsequent pointed observations were then carried out towards this peak location of the methanol emission.

¹ This publication is based on data acquired with the Atacama Pathfinder EXperiment (APEX). APEX is a collaboration between the Max-Planck-Institut für Radioastronomie, the European Southern Observatory, and the Onsala Space Observatory.

The band pass shape was calibrated using either position switching with ~ 30 seconds on or off time or in wobbler mode, which observes the reference at a $90''$ offset in azimuth at a rate of 0.7 Hz. A frequency dependent beam efficiency was adopted (see Table 1) for APEX-1 (Vassilev et al. 2008). For FLASH, a fixed value of $\eta_{\text{mb}} = 0.70$ was used. The forward efficiency value of $f_{\text{eff}} = 0.95$ was used for the whole frequency range. Both of these values for FLASH were based on the information provided on the instrument's webpage.²

Table 1. Summary of frequency setups used during the observations.

Instrument	ν (GHz)	σ_{rms} (K)	η_{mb}	Beam ('')
APEX-1	213-217	0.01	0.82	30
	216-220	0.01	0.82	29.5
	220-224	0.01	0.80	29
	224-228	0.02	0.80	28.5
	234-238	0.02	0.78	27.5
	238.5-242.5	0.02	0.76	27
	242-246	0.01	0.76	26.5
	245-249	0.01	0.76	26
	248-252	0.02	0.74	25.5
	251-255	0.02	0.74	25
	288.5-292.5	0.01	0.70	21
	292.5-296.5	0.02	0.70	21
	296.5-300.5	0.01	0.70	20.5
	300.5-304.5	0.01	0.70	20.5
FLASH	304.5-308.5	0.02	0.70	20
	308.5-312.5	0.01	0.70	20
	334-338	0.02	0.70	18.5
	339-343	0.03	0.70	18
	343-347	0.02	0.70	18
	346-350	0.02	0.70	17.5
	349-353	0.02	0.70	17.5
	351-355	0.02	0.70	17.5
	355-359	0.02	0.70	17
	358-362	0.01	0.70	17
	361-365	0.02	0.70	17
	370-374	0.02	0.70	16.5

Notes. Columns are, left to right, receiver, covered frequency range, rms noise at a velocity resolution of ~ 1.0 km s $^{-1}$, main-beam efficiency and FWHM beam width.

2.2. Data reduction

The data analysis was done using the GILDAS package³. All the scans with identical backend tuning frequency were stacked channel by channel and then averaged. The frequency ranges of each pair of overlapping backend modules were stitched together and boxcar smoothed to a resolution of ~ 1.0 km s $^{-1}$ to provide a single spectrum for the whole 4 GHz receiver bandwidth. Emission lines with peak main-beam brightness temperature, T_{MB} , greater than 3σ at 1.0 km s $^{-1}$ resolution were considered as detection. For each candidate emission line, a baseline was subtracted with 100 channels on either side of the profile. In most of the cases, a first-order baseline was fitted. In about $\sim 20\%$ of the cases we had to fit a second-order baseline.

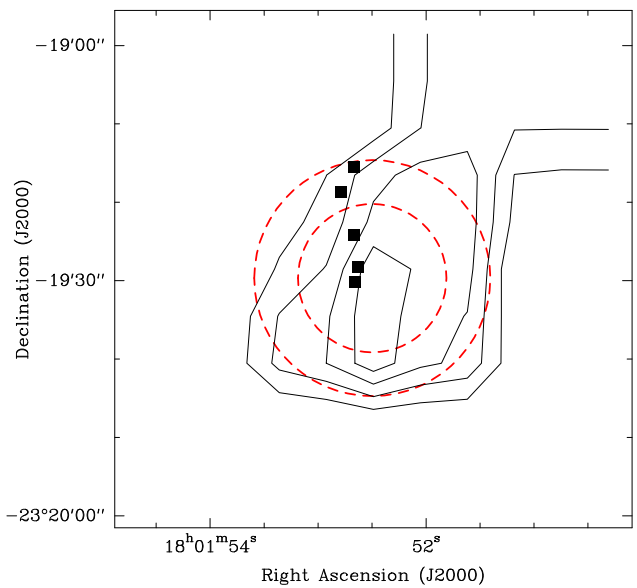


Fig. 2. W28 F: Map of the main-beam brightness temperature of the CH_3OH ($J = 6_0 - 5_0 A^+$) transition integrated over the LSR velocity range from -10 to 25 km s $^{-1}$. The contour values are at three, five, seven and nine times the rms noise level, which is 0.36 K km s $^{-1}$. Overlaid we have the OH maser positions (black filled squares) from Claussen et al. (1997) that are located inside the field of view. The large and small circles ($30''$ and $16''$ diameter) represent the FWHM beam width of the APEX telescope at our lowest and highest observing frequency (213 and 374 GHz, respectively). The beams are centered on the methanol peak position (see text) toward which we performed our long integrations.

3. Analysis and results

3.1. Molecules detected in W28 F

The averaged, smoothed, and baseline subtracted spectra were used to identify the spectral lines. For this purpose, we used the JPL spectral line catalog⁴ (Pickett et al. 1998) and the Cologne Database for Molecular Spectroscopy (CDMS) (Müller et al. 2005). We detected multiple lines of H_2CO , CH_3OH , SO , SiO , CS , CN , CCH , and NO as well as many other molecular species including CO and its isotopologues, HCO^+ , H^{13}CO^+ , HCN , HNC , and N_2H^+ . This is the first detection of thermally excited CH_3OH emission in an SNR, while methanol maser detections in SNRs have been reported before (Pihlström et al. 2014). For some molecules, such as H_2CO and CH_3OH there are several transitions close together in frequency space that have been observed simultaneously. This facilitates accurate determination of temperature and densities without significant calibration and beam-filling factor uncertainties. Figure 3 shows some of the detected lines of CH_3OH , H_2CO , SO and SiO . The other detected lines are presented in Fig. A.1. After identification, a Gaussian profile was fitted to each of them to obtain the following line parameters: local standard of rest (LSR) velocity (V_{LSR}), line width (ΔV), peak main-beam temperature (T_{MB}), and the integrated intensity ($\int T_{\text{MB}} dv$). A single Gaussian turned out to be

² <https://www.mpifr-bonn.mpg.de/4482467/calibration>

³ <http://www.iram.fr/IRAMFR/GILDAS>

⁴ <https://spec.jpl.nasa.gov/home.html>

Table 2. Observed molecular species of W28 F and the resulting line parameters from a single Gaussian fit.

Species	Transition	Frequency (MHz)	E_{up} (K)	$\int T_{\text{MB}} \, dv$ (K km s ⁻¹)	V_{LSR} (km s ⁻¹)	ΔV (km s ⁻¹)	T_{MB} (K)
p-H ₂ CO	$3_{0,3} - 2_{0,2}$	218222.192	21.0	3.94(7)	6.7(1)	11.0(2)	0.34(1)
	$3_{2,2} - 2_{2,1}$	218475.632	68.1	0.99(6)	6.9(3)	9.9(7)	0.09(1)
	$3_{2,1} - 2_{2,0}$	218760.066	68.1	1.29(7)	6.8(3)	10.6(8)	0.11(1)
	$4_{0,4} - 3_{0,3}$	290623.405	34.9	3.34(7)	7.1(1)	9.6(2)	0.33(2)
	$4_{2,3} - 3_{2,2}$	291237.766	82.1	1.01(7)	7.8(3)	9.4(8)	0.10(2)
	$4_{2,2} - 3_{2,1}$	291948.067	82.1	0.97(7)	6.7(3)	8.3(8)	0.11(2)
	$5_{0,5} - 4_{0,4}$	362736.048	52.3	1.3(1)	7.2(5)	12(2)	0.10(2)
	$3_{1,2} - 2_{1,1}$	225697.775	33.4	4.6(2)	6.9(2)	10.7(5)	0.40(2)
	$4_{3,2} - 3_{3,1}$	291380.442	140.9	1.02(6)	-	-	0.08(2) ^a
o-H ₂ CO	$4_{3,1} - 3_{3,0}$	291384.361	140.9	1.02(6)	-	-	0.08(2) ^a
	$4_{1,3} - 3_{1,2}$	300836.635	47.9	4.36(8)	6.96(9)	10.1(2)	0.40(2)
	$5_{1,5} - 4_{1,4}$	351768.645	62.5	3.2(1)	7.0(2)	12.2(5)	0.25(2)
	$4_2 - 3_1 E$	218440.063	45.5	0.72(1)	7.2(7)	9(2)	0.07(1)
	$5_0 - 4_0 E$	241700.159	47.9	1.0(4)	6(2)	10(4)	0.10(2)
	$5_{-1} - 4_{-1} E$	241767.234	40.4	4.1(1)	7.0(1)	10.5(4)	0.37(2)
	$5_1 - 4_1 E$	241879.025	55.9	-	-	-	< 0.06 ^b
	$5_{-2} - 4_{-2} E$	241904.147	60.7	0.34(8)	-	-	0.03(2) ^a
	$5_2 - 4_2 E$	241904.643	57.1	0.34(8)	-	-	0.03(2) ^a
E-CH ₃ OH	$6_0 - 5_0 E$	289939.377	61.8	1.0(1)	6.3(4)	10(1)	0.10(2)
	$6_{-1} - 5_{-1} E$	290069.747	54.3	4.13(8)	7.28(9)	9.5(2)	0.41(2)
	$6_1 - 5_1 E$	290248.685	69.8	-	-	-	< 0.06 ^b
	$6_{-2} - 5_{-2} E$	290307.281	74.7	0.33(6)	-	-	0.03(1) ^a
	$6_2 - 5_2 E$	290307.738	71.0	0.33(6)	-	-	0.33(1) ^a
	$3_0 - 2_{-1} E$	302369.773	27.1	0.86(7)	7.4(3)	8.4(8)	0.10(2)
	$3_1 - 2_0 E$	310192.994	35.0	0.51(7)	8.1(6)	9(1)	0.05(1)
	$4_0 - 3_{-1} E$	350687.662	36.3	-	-	-	~ 0.07(1) ^c
	$5_0 A^+ - 4_0 A^+$	241791.352	34.8	4.8(1)	7.1(1)	9.7(2)	0.47(2)
	$5_2 A^- - 4_2 A^-$	241842.284	72.5	-	-	-	< 0.06 ^b
	$5_2 A^+ - 4_2 A^+$	241887.674	72.5	-	-	-	< 0.06 ^b
	$6_0 A^+ - 5_0 A^+$	290110.637	48.7	5.60(8)	7.19(6)	9.6(2)	0.54(2)
	$1_1 A^- - 1_0 A^+$	303366.921	16.9	0.68(9)	7.2(6)	10(2)	0.06(2)
	$2_1 A^- - 2_0 A^+$	304208.348	21.6	0.64(8)	6.2(6)	9(1)	0.06(2)
	$3_1 A^- - 3_0 A^+$	305473.491	28.6	0.95(7)	6(1)	14(2)	0.06(1)
A-CH ₃ OH	$4_1 A^- - 4_0 A^+$	307165.924	38.0	0.68(8)	7.6(4)	11(1)	0.08(1)
	$5_1 A^- - 5_0 A^+$	309290.360	49.7	0.67(7)	6(1)	10(1)	0.06(2)
	$6_1 A^- - 6_0 A^+$	311852.612	63.7	0.58(7)	6.9(4)	6.7(9)	0.08(1)
	$1_1 A^+ - 0_0 A^+$	350905.100	16.8	0.70(8)	7.4(8)	14(2)	0.05(1)
	$5_5 - 4_4$	215220.653	44.1	1.30(9)	6.3(3)	11.8(7)	0.11(2)
	$6_5 - 5_4$	251825.770	50.7	1.4(1)	7.4(5)	10(1)	0.12(3)
	$7_7 - 6_6$	301286.124	71.0	0.80(8)	6.9(4)	9(1)	0.09(2)
	$7_8 - 6_7$	304077.844	62.1	2.4(1)	7.2(2)	11.8(7)	0.19(2)
	$8_8 - 7_7$	344310.612	87.5	0.8(1)	6(1)	10(2)	0.07(2)
SO	$8_9 - 7_8$	346528.481	78.8	1.4(1)	6.7(5)	9(1)	0.14(1)
	$5 - 4$	217104.919	31.3	2.45(7)	7.0(2)	12.7(4)	0.18(1)
	$7 - 6$	303926.960	58.3	1.01(8)	6.5(4)	11(1)	0.09(2)
SiO	$8 - 7$	347330.581	75.0	1.0(1)	8.1(8)	14(2)	0.06(1)

Notes. Columns left to right: molecular species, quantum numbers, frequency and upper level energy of transition, velocity-integrated main-beam brightness temperature, centroid LSR velocity, line width, and peak main-beam brightness temperature. The T_{MB} values are the fit results and not the absolute peak observed values. In cases where no Gaussian fitting could be done, the observed temperature peaks have been shown. The numbers within the parentheses show the error associated with the last significant digit.

(^a) These lines were blended with same E_{up} and A_{ij} values. They were fitted with one Gaussian and the integrated intensities were obtained by dividing the result of the fit by the number of blended lines assuming equal contribution from each. No attempt was made to derive LSR velocities or line widths.

(^b) 3σ detection threshold applied for non-detected lines.

(^c) The covered CH₃OH lines were blended with a NO line and hence only an estimate of the upper limit on their peak main-beam brightness temperature could be established. For this, we assumed that the NO lines at ~351050 and ~350690 MHz have similar emission strengths because of their identical E_{up} and very similar A_{ij} values.

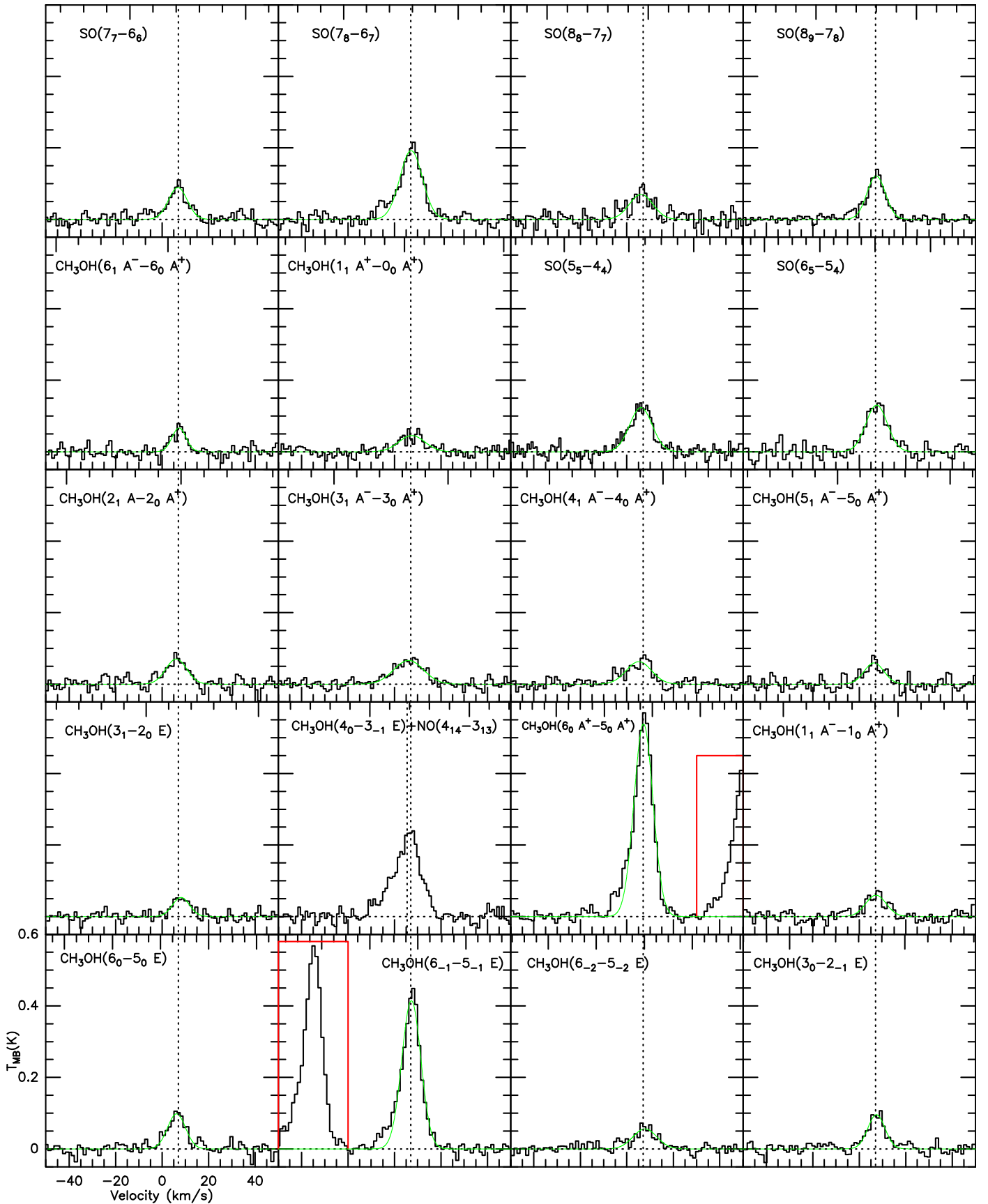
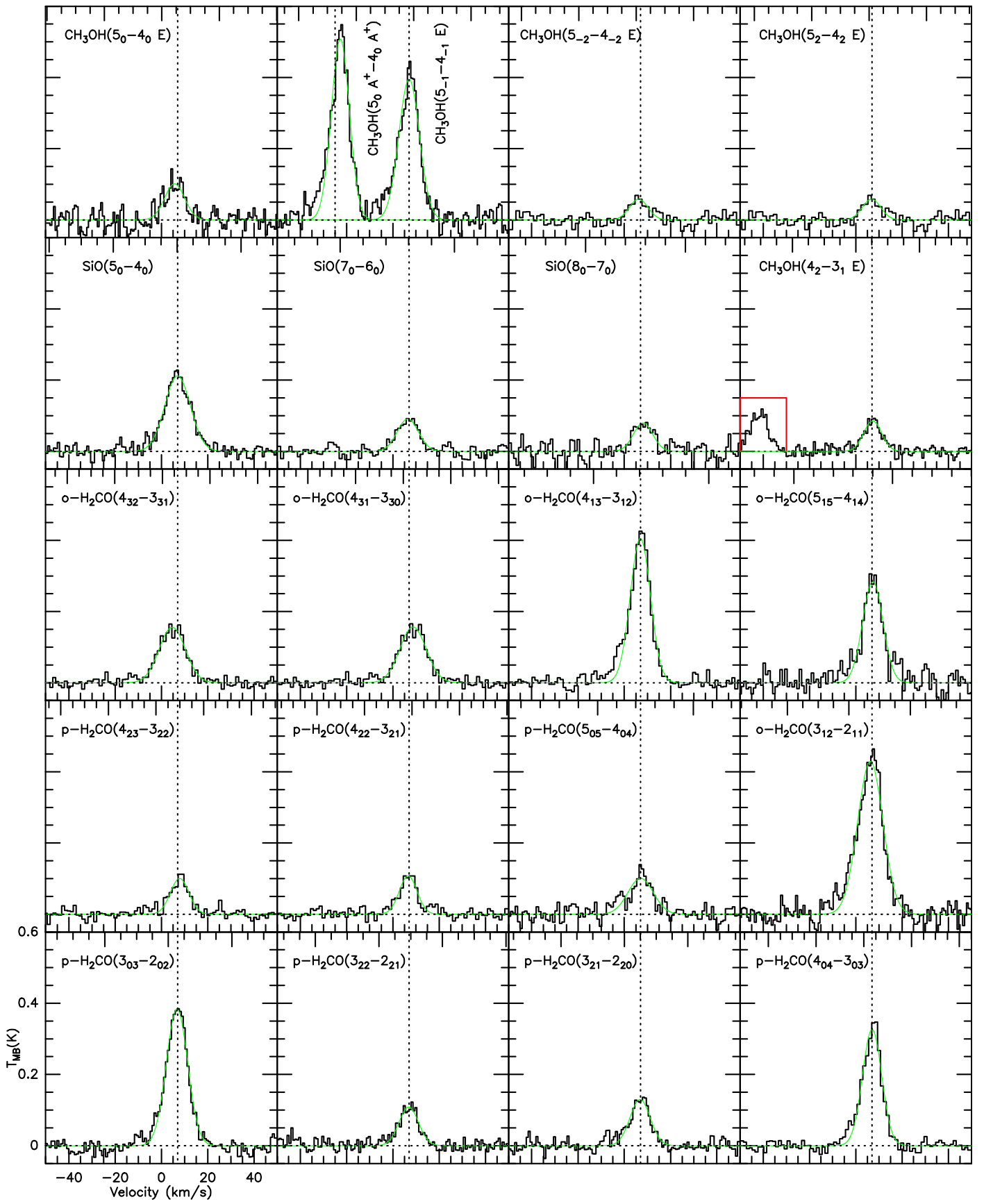


Fig. 3. Spectra of the observed species in W28 F. The intensity is in the T_{MB} scale. The LSR velocity scale in km s^{-1} , is appropriate for the line listed in the upper left corner of each panel, except for cases in which more than one line is shown, which are explicitly labelled. Lines marked with red lines are not labelled in the shown window. All the spectra have been smoothed to a velocity resolution of $\approx 1 \text{ km s}^{-1}$. Single gaussian fits are shown as green lines overlaid on the spectra. Dashed vertical lines are at an LSR velocity of 7 km s^{-1} for the labeled lines.

**Fig. 3.** continued ..

adequate to fit all the spectral lines except for the lines of CO and its isotopologues which displayed more complex profiles includ-

ing self-absorption. For molecular species with multiple detected lines very closely spaced in frequency, the resulting line profile was non-Gaussian. Thus, no Gaussian fitting was done for such species and only upper limits on their emission were determined from peak T_{MB} values. Table 2 lists the spectral lines shown in Fig. 3 with their respective line parameters obtained from the fit. Other molecular line fit parameters are shown in Table B.1.

3.2. Kinematics

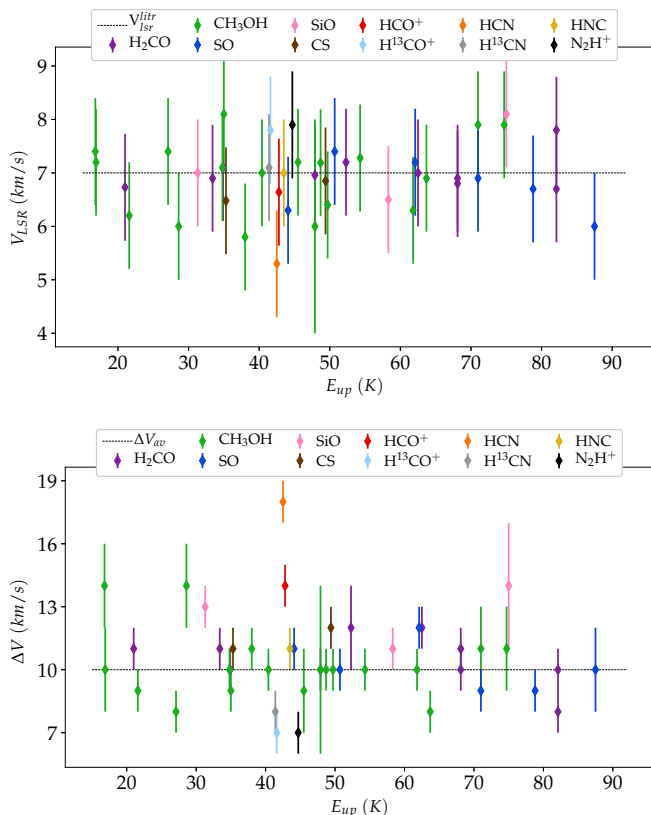


Fig. 4. Scatter plots for LSR velocity, V_{LSR} , (top) and line widths, ΔV , (bottom) for detected lines of different species in W28 F.

Figure 4 shows scatter plots of the LSR velocities (upper panel) and line widths (lower panel) of all detected lines as a function of the upper energies above ground state, E_{up} , of the transitions (see Tab. 2). There does not seem to be any particular dependence of either quantity on E_{up} . The LSR velocities are scattered around $\sim 7 \text{ km s}^{-1}$. This is in agreement with W28's V_{LSR} values found in the literature (Arikawa et al. 1999; Fukui 2008; Velázquez et al. 2002; Reach et al. 2005b). Line widths are found in the range from 7 to 18 km s^{-1} , with most of the lines close to 10 km s^{-1} , indicating that they originate from the post-shock gas. Many plausible reasons may contribute to a large scatter in line widths. First, transitions with a low signal-to-noise ratio (S/N), e.g. CH_3OH ($1_1 \text{A}^+ - 0_0 \text{A}^+$) at 350905.100 MHz and SiO ($8 - 7$) at 347330.581 MHz , have a large uncertainty in their fitted line width values. Second, species such as HCN and HCO^+ are more abundant compared to others. Consequently, their emission lines are much stronger and have detectable broad wings. Their less abundant isotopologues like H^{13}CN and H^{13}CO^+ on the other hand, emit lines that are much weaker and, hence, do not have detectable wings. Third, lines from HCN and HCO^+ could also be broadened because of their high optical depths. Fi-

nally, species such as N_2H^+ may be tracing the ambient medium and, hence, demonstrate narrow line widths.

In addition, we also checked that the hyperfine structure splitting for the (4–3) transitions of HCN , H^{13}CN , N_2H^+ , and HNC and the relative intensities of the satellites are too small to have a measurable effect on the profiles of lines with a typical width of 10 km s^{-1} . Hereafter, we adopt $V_{\text{LSR}} \sim 7 \text{ km s}^{-1}$ and $\Delta V \sim 10 \text{ km s}^{-1}$.

4. Modeling molecular line intensities : Physical conditions

We used multiple lines from different species that we observed to probe the physical conditions in W28 F region. We used RADEX⁵ (van der Tak et al. 2007) to model the observed line integrated intensity, which is a statistical equilibrium radiative transfer code made available for public use. It is a useful tool that provides constraints on physical conditions, namely density and kinetic temperature. RADEX computes the excitation of the molecular lines under non-LTE conditions, provided their collisional rate coefficients are available. It estimates line intensities using the escape probability formulation. In order to calculate the escape probabilities, we use the Large Velocity Gradient (LVG) approximation (Sobolev 1960; Surdej 1977). Under this approximation the emitted line photons can escape as long as the velocity shift resulting from the velocity gradient is larger than the local line thermal width, which is valid in C-type shocks (see e.g., Gusdorf et al. 2008). Other assumptions used in RADEX modeling include the source being an isothermal and homogeneous sphere filling the beam of the telescope. A detailed description of our RADEX analysis is described in the Appendix C.

Since all the observations were done towards the direction of brightest emission from CH_3OH lines at 290 GHz near the OH maser regions, our data lacks the scope to allow us to determine the extent of the molecular emission. Looking at the extended nature of CO emissions mapped by Frail & Mitchell (1998) (see their Fig. 1a) and Gusdorf et al. (2012) (see their Fig. 1), we may assume that the emission from other molecules is also extended in nature, which would correspond to a beam-filling factor of 1. However, this assumption may not be entirely true, in which case, a beam dilution factor needs to be assumed. Apart from the standard calibration error associated with APEX data, this unknown beam-filling factor is the largest source of uncertainty when scaling line intensities to account for differences in beamsize caused by different observing frequencies. In order to quantify how this impacts the results, all the analyses presented throughout this paper were carried out for two extreme cases: a point like source and an extended source covering the whole beam. The results obtained for a point-like source were not significantly different from those of the extended source when a 20% uncertainty was assumed while scaling the line intensities for the latter. Therefore, all results presented in this paper correspond to the case of an extended source with a beam-filling factor of 1 along with a 20% uncertainty added while scaling intensities to account for differences in beam size.

4.1. Formaldehyde

Formaldehyde (H_2CO), a slightly asymmetric rotor molecule, is a ubiquitous molecule in interstellar clouds and exhibits a large number of millimetre and sub-millimetre transitions. Previous

⁵ <http://www.sron.rug.nl/~vdtak/radex/index.shtml>

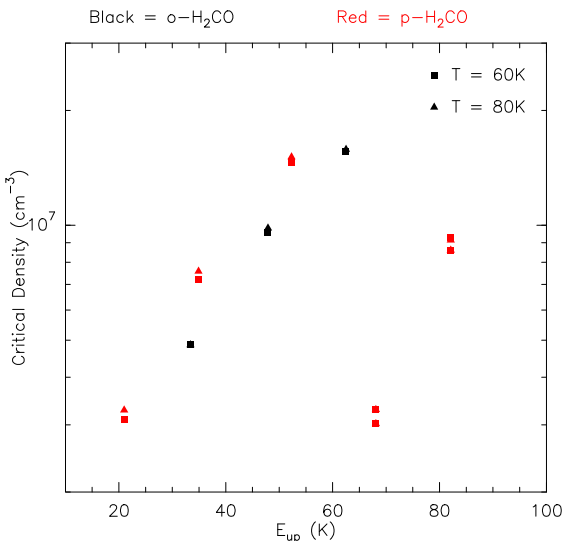


Fig. 5. Critical density versus upper level energy scatter plot of observed o-H₂CO (black symbols) and p-H₂CO (red symbols). Collisions only with H₂ at 60 K (square) and 80 K (triangle) have been used to derive the critical densities.

observations of H₂CO in various molecular environments indicate that it is a reliable tracer of physical conditions of dense gas (see Mangum & Wootten 1993a; Ginsburg et al. 2011; Ao et al. 2013; Ginsburg et al. 2016a,b; Tang et al. 2017a,b, 2018a,b; Mangum et al. 2019).

The peak intensity of emission lines depend on the kinetic temperature (T_{kin}), density of collision partners (e.g. n_{H_2}) and column density ($N(\text{H}_2\text{CO})$) of the molecule. However, when the density of the colliding partner (e.g., H₂) is higher than the critical density of the molecule, the collisions will be frequent enough to populate the energy levels of the molecule according to the Boltzmann distribution law. Consequently, the intensity of emission will only be a function of temperature and column density. The critical density of a transition from level i to level j is defined by

$$n_{\text{crit}_{ij}} = A_{ij}/C_{ij}, \quad (1)$$

where A_{ij} is the Einstein A coefficient and C_{ij} is the collisional rate coefficient in $\text{cm}^3 \text{ s}^{-1}$.

Using the intensities of individual H₂CO lines to constrain the kinetic temperature and spatial densities can be error-fraught due to large absolute calibration uncertainties and beam-filling factor. Thus, we opted to use line ratios instead. The relative populations of the H₂CO rotational energy levels in different K_a ladders are predominantly governed by collisions since dipole selection rules dictate that $\Delta K = 0$ for radiative excitation; hence, ratios of line fluxes involving different K_a ladders are good tracers of the kinetic temperature. On the other hand, line ratios involving lines emitted from within the same K_a ladders yield estimates of the spatial density of the gas (Mangum & Wootten 1993a). We excluded the collisions with electrons and atomic hydrogen in our RADEX analysis because they are not expected to have a significant contribution in comparison to H₂. The abundance ratio of electrons ($x(e) = n(e)/n(\text{H}_2) \lesssim 10^{-5}$) should not be large given that the gas has undergone a C-type shock (Gusdorf et al. 2012). Observations of W28 by Velázquez et al. (2002) showed that overall molecular hydrogen is at least three times more abundant than H I in the SNR as a whole. Hence, neglecting collisions with electrons and hydrogen atoms is justified. Nevertheless, van Dishoeck et al. (1993) did not find a significant dif-

ference in results from including collisions from these species in their similar analysis of SNR IC 443 either.

Figure 5 shows the critical densities of H₂CO lines observed in W28 F. The values of the collisional coefficients have been taken from the Leiden Atomic and Molecular Database (LAMDA)⁶ (Schöier et al. 2005). The C_{ij} value adopted for Fig. 5 corresponds to $T_{\text{kin}} = 60$ K, with a caution that C_{ij} varies as a function of the kinematic temperature. However, the lowest derived critical density for a range of $50 < T_{\text{kin}} < 100$ K is $\sim 1 \times 10^6 \text{ cm}^{-3}$ and the dependence of C_{ij} on kinetic temperature is likely insignificant for H₂CO (see Fig. 5). Since the critical densities of the observed lines can reach up to $\sim 2 \times 10^7 \text{ cm}^{-3}$, the LTE condition is most likely not satisfied. Hence, non-LTE modeling of the emission is required to constrain the physical conditions existent in W28 F from formaldehyde emission lines.

Many pairs of H₂CO transitions can be measured simultaneously with the same receiver system and angular resolution. Being able to simultaneously observe multiple lines means the calibration uncertainties are largely reduced. Additionally, taking their flux ratio eliminates the uncertainties related to unknown beam-filling factors. In this work, we used the lines ratios $3_{22}-2_{21}/3_{03}-2_{02}$, $3_{21}-2_{20}/3_{03}-2_{02}$, $4_{23}-3_{22}/4_{04}-3_{03}$, and $4_{22}-3_{21}/4_{04}-3_{03}$ of p-H₂CO to constrain the kinetic temperature. The density was constrained using the $4_{04}-3_{03}/3_{03}-2_{02}$ and $5_{05}-4_{04}/3_{03}-2_{02}$ line ratios of p-H₂CO as well as $5_{15}-4_{14}/3_{12}-2_{11}$ and $4_{13}-3_{12}/3_{12}-2_{11}$ of o-H₂CO. The intensity ratios were modeled on a 2 dimensional grid of kinetic temperature (T_{kin}) and H₂ density ($n(\text{H}_2)$) for a fixed of column density for both ortho- and para-H₂CO, whose effect will be considered later. The grid points were logarithmically distributed over the range of variables as listed in Table C.1. A value of $\Delta V = 10 \text{ km s}^{-1}$ was used throughout. The background temperature was assumed to be that of the CMB, $T_{\text{CMB}} = 2.73$ K.

Figure 6 shows the results of the RADEX modeling on the line ratios for $N(\text{H}_2\text{CO}) = 10^{13} \text{ cm}^{-2}$. Firstly, the optical depth is less than 0.5 for all lines so that the extinction is rather small and could be neglected. Secondly, the gas number density is constrained as $n(\text{H}_2) \simeq 1 - 5 \times 10^6 \text{ cm}^{-3}$ (see top panel). However, the line ratio of $5_{15}-4_{14}/4_{13}-3_{12}$ does not constrain the density very well. We note that the density constraints obtained from the observed line ratios for p-H₂CO are consistent with those obtained from o-H₂CO. So, both these lines are also most likely originating from a similar region. Lastly, RADEX constrains the kinetic temperatures as $T_{\text{kin}} \sim 50 - 80$ K with $n_{\text{H}_2} > 10^6 \text{ cm}^{-3}$ (see bottom panel). However, the ratio of $3_{21}-2_{20}/3_{03}-2_{02}$ results in a higher constraint of T_{kin} . Such high values of kinetic temperature in addition to broad line widths also indicate that the emission is originating from the post-shock gas.

The column density was then varied from 10^{12} to 10^{14} cm^{-2} , but no significant change in the results was seen. For these estimates of the kinetic temperature and the gas number density, we estimated the column density of $N(\text{p-H}_2\text{CO}) \sim 0.3 - 1 \times 10^{13} \text{ cm}^{-2}$ and $N(\text{o-H}_2\text{CO}) \sim 0.5 - 2.5 \times 10^{13} \text{ cm}^{-2}$ from 99.7% confidence level contours in Fig. 7.

4.2. Methanol

Methanol exists in two separate species, namely A-type CH₃OH and E-type CH₃OH. All transitions from one to the other via collisions are forbidden, and de facto, as in the cases of ortho- and para-H₂CO, they are treated as independent species. Figure 8 shows the critical densities of the observed A- and E-CH₃OH

⁶ <http://home.strw.leidenuniv.nl/~moldata/>

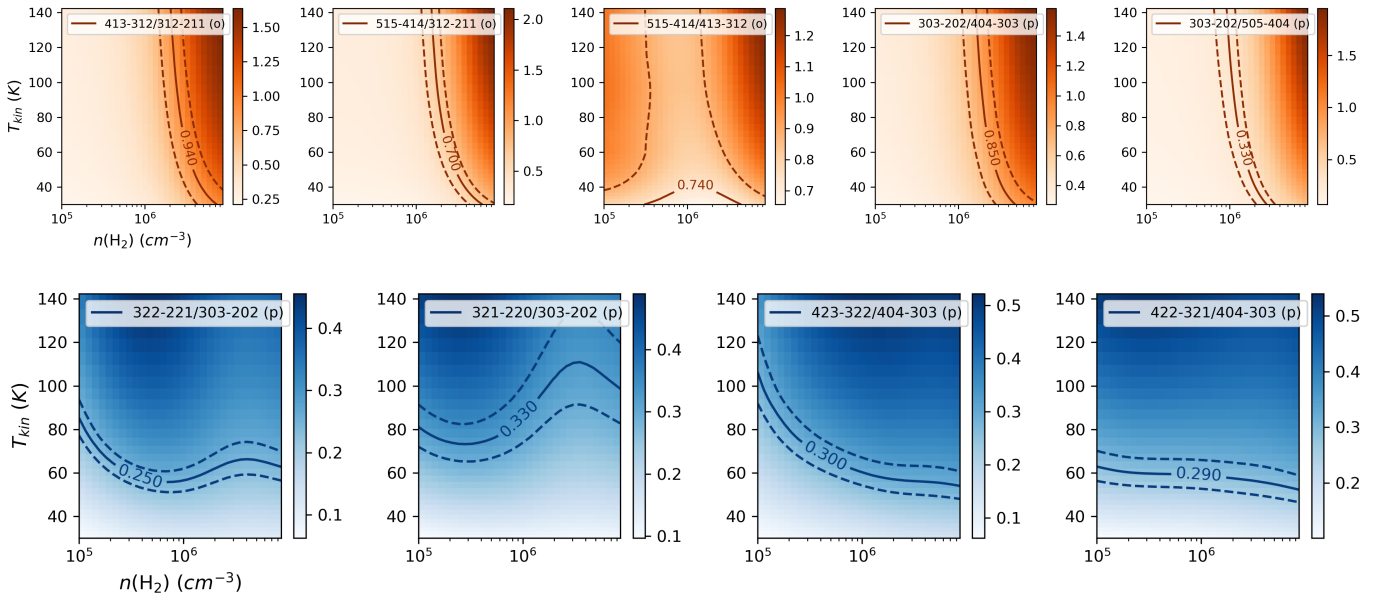


Fig. 6. RADEX non-LTE modeling of the H₂CO line ratios to probe H₂ spatial-density (top) and kinetic temperature (bottom). The background color shows the modeled ratios on the density and temperature grid. Solid lines are the contours of modeled ratios corresponding to the observed values and dashed lines correspond to the uncertainties. Adopted value of column density for these contours is $N = 10^{13} \text{ cm}^{-2}$. The effects of optical depths were monitored during the modeling and they are smaller than 0.3 and hence do not effect the results significantly.

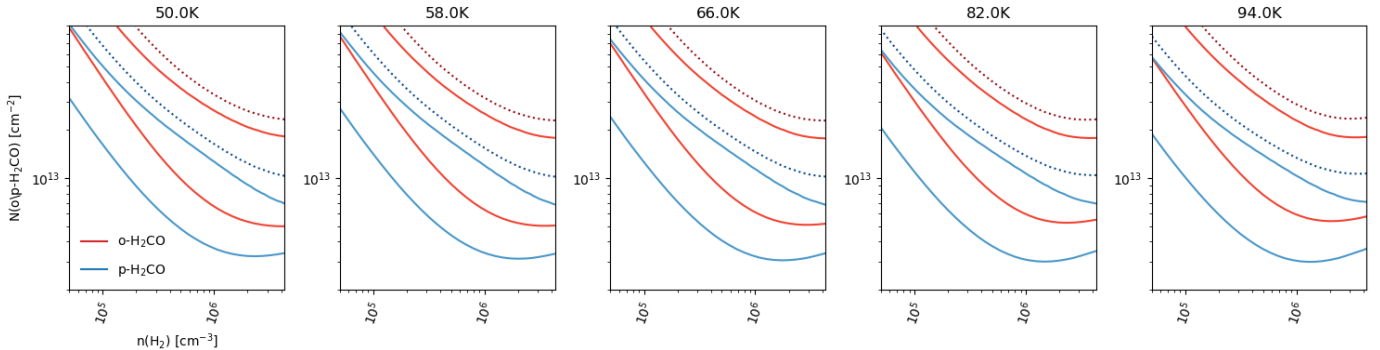


Fig. 7. RADEX non-LTE modeling of the line intensity of o- and p-H₂CO to probe the column densities of both species. Each panel corresponds to a slice of constant T_{kin} from a 3D grid of $\bar{\sigma}^2$ (see Appendix C). Red contours are for o-H₂CO, while blue ones are for p-H₂CO. The solid and dotted contours are represented by 99.7% and 99.99% that the observed intensity inside the modeled contours (or $\bar{\sigma}^2 = 9$ and 25), respectively.

lines at $T_{\text{kin}} = 60$ and 80 K, considering only H₂ collisions. Multiple transitions have a critical density of $1 - 5 \times 10^7 \text{ cm}^{-3}$. Thus, a non-LTE RADEX model is needed. The grid is listed in Table C.1. Similarly to the case of formaldehyde, we used the ratios of lines to constrain on the kinetic temperatures and the gas number densities. However, the CH₃OH lines are far apart in frequency and were not observed simultaneously. Therefore, the associated calibration and filling factor uncertainties cannot be eliminated.

Leurini et al. (2004) demonstrated that the $5_k - 4_k$ and $7_k - 6_k$ line ratios of CH₃OH at 241 GHz and 338 GHz are sensitive enough to probe the dense gas, with density higher than 10^5 cm^{-3} . Our observations did not cover the frequencies of the $7_k - 6_k$ series. Hence we could only use the E-CH₃OH $5_{-1} - 4_{-1}$ E/ $5_0 - 4_0$ E at 240 GHz along with the $6_{-1} - 5_{-1}$ E/ $6_0 - 5_0$ E line ratio at 290 GHz instead. Figure 9 shows the contours of observed line ratios modeled from RADEX with a fixed column

density of $N = 7 \times 10^{13} \text{ cm}^{-2}$ (varying the column density value over the overlapping 3σ range from Fig. 10 did not change the results significantly). Both line ratios are not sensitive to the kinetic temperature. However, if we adopt the kinetic temperature in the range of $50 < T_{\text{kin}} < 80$ K from the formaldehyde analysis, the density value is constrained to $n(\text{H}_2) = 2_{-1}^{+4} \times 10^6 \text{ cm}^{-3}$. This is in agreement with the result inferred from the H₂CO. Hence, the emission is probably originating from the same cloud.

The observed lines intensities as described in Table 2 were used to probe the CH₃OH column density. Figure 10 shows the contours constraining the observed line intensities of CH₃OH on an $N(\text{CH}_3\text{OH})$ versus n_{H_2} grid for different values of T_{kin} . With $T_{\text{kin}} = 60$ K and $n_{\text{H}_2} = 2 \times 10^6 \text{ cm}^{-3}$, the 3σ contours (99.7% confidence level) of A- and E-CH₃OH indicate a column density of $4 \times 10^{13} \lesssim N(\text{E-CH}_3\text{OH}) \lesssim 1.5 \times 10^{14} \text{ cm}^{-2}$ and $2 \times 10^{13} \lesssim N(\text{A-CH}_3\text{OH}) \lesssim 8 \times 10^{13} \text{ cm}^{-2}$.

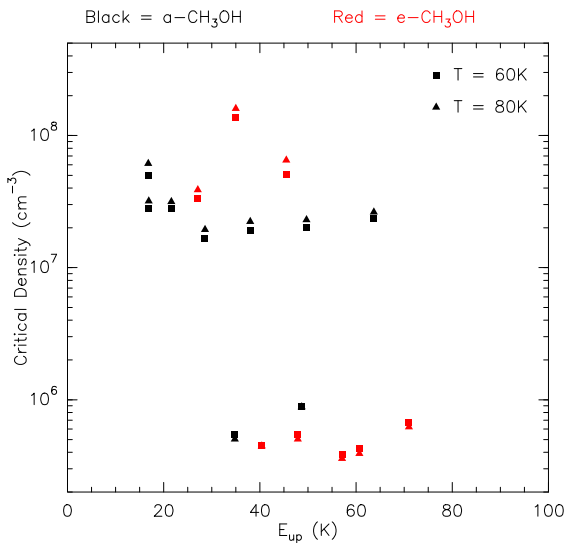


Fig. 8. Critical density vs. upper level energy plot for the observed transitions of CH_3OH . The collisional coefficient is achieved by only H_2 collider.

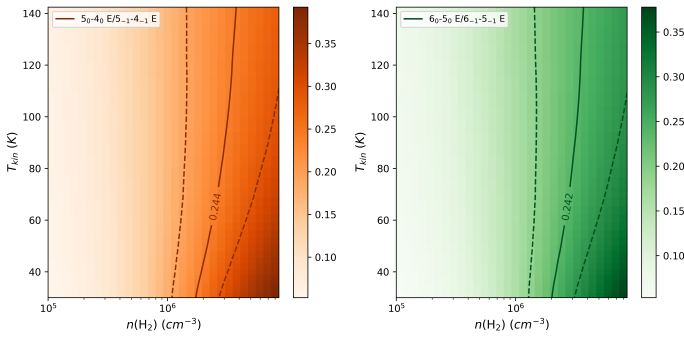


Fig. 9. RADEX non-LTE modeling of the CH_3OH line ratios to probe H_2 spatial-density. The solid lines are the observed values and dashed lines correspond to the uncertainties. The adopted value of column density used to produce these contours is $N = 7 \times 10^{13} \text{ cm}^{-2}$.

4.3. Other molecular lines

We also attempted to use the other multiple transitions of SO, SiO, and CS towards W28 F. Similarly, we first calculated the critical densities with collision partner H_2 which results in the lowest critical density of $2.4 \times 10^6 \text{ cm}^{-3}$ corresponding to the SO ($J = 5_5 - 4_4$) line. Hence, these lines were also modeled using the non-LTE RADEX code. However, the results appear to be independent of the choice of kinetic temperature over the range of modeled values (see Fig. D.1). Other species with one single emission line detected, for instance, HCO^+ , H^{13}CO^+ , HCN, and HNC, RADEX could not also provide explicit constraints on the kinematic temperature, gas density, and their column density. Therefore, we made the assumption that all line emissions are originating from the same physical conditions as H_2CO , which allowed us to derive the column density of these molecules for $T_{\text{kin}} = 58 \text{ K}$ and $n(\text{H}_2) = 2 \times 10^6 \text{ cm}^{-3}$. The results are listed in Table 3.

Table 3. Column densities of observed species in W28 F.

Molecule	$N (\text{cm}^{-2})$
p- H_2CO	$0.3-1 \times 10^{13}$
o- H_2CO	$0.5-2.5 \times 10^{13}$
E- CH_3OH	$0.4-1.4 \times 10^{14}^a$
A- CH_3OH	$1-8 \times 10^{13}^a$
SO	$1-3 \times 10^{13}^a$
SiO	$1-4 \times 10^{12}^a$
CS	$0.5-2 \times 10^{13}^a$
HCO^+	$0.3-1 \times 10^{13}^a$
H^{13}CO^+	$0.8-3 \times 10^{11}^a$
HCN	$1-5 \times 10^{13}^a$
HNC	$0.8-2 \times 10^{12}^a$

Notes. ^(a) For an assumed kinetic temperature $T_{\text{kin}} = 58 \text{ K}$ and a spatial density $n(\text{H}_2) = 2 \times 10^6 \text{ cm}^{-3}$.

5. Discussion

5.1. Molecular composition

In this section, we estimate the abundances of our detected molecules. In order to estimate molecular abundances, we need to know the H_2 column density in W28 F. We adopt the value constrained by [Gusdorf et al. \(2012\)](#), in which the authors used non-dissociative shock modeling to estimate $N(\text{CO})$ as $1.9 \times 10^{18} \text{ cm}^{-2}$. Assuming a “standard” ISM CO abundance of $[\text{CO}]/[\text{H}_2] = 10^{-4}$ (see [Bolatto et al. 2013](#)), the H_2 column density is $N(\text{H}_2) = 1.9 \times 10^{22} \text{ cm}^{-2}$. We note that, in the presence of dissociative shocks, both CO and H_2 can be destroyed and, depending on their reformation pathway, this abundance value can change.

Table 4. Abundances of observed species in W28 F.

Molecule	W28 F	IC 443 ^a	TMC-1 ^b
H_2CO	$0.4-1.8 \times 10^{-9}$	4×10^{-9}	2×10^{-8}
CH_3OH	$0.3-1.1 \times 10^{-8}$	$< 1 \times 10^{-10}$	2×10^{-9}
SO	$0.5-1.6 \times 10^{-9}$	8×10^{-9}	$> 7 \times 10^{-9}$
SiO	$0.5-2.1 \times 10^{-10}$	8×10^{-10}	$< 2 \times 10^{-12}$
CS	$0.3-1.0 \times 10^{-9}$	3×10^{-9}	$> 5 \times 10^{-9}$
HCO^+	$1.6-5.2 \times 10^{-10}$	3×10^{-9}	8×10^{-9}
H^{13}CO^+	$0.4-1.6 \times 10^{-11}$	$< 1 \times 10^{-10}$	2×10^{-10}
HCN	$0.5-2.6 \times 10^{-9}$	8×10^{-9}	2×10^{-8}
HNC	$0.4-1.0 \times 10^{-10}$	1×10^{-9}	2×10^{-8}

Notes. ^(a) Towards clump G I ([van Dishoeck et al. 1993](#)). ^(b) [Gratier et al. \(2016\)](#); [Ohishi et al. \(1992\)](#) and references in Table 8 of [van Dishoeck et al. \(1993\)](#) for SiO, H^{13}CO^+ .

The results are shown in Table 4. Furthermore, we compare them to what was found for another well-known SNR, IC443 by [van Dishoeck et al. 1993](#) and the dark cloud TMC-1 (an unshocked region), reported in [Gratier et al. 2016](#), and references therein for a same range of observed frequencies. The comparisons show that (1) the abundances of molecules in W28 F derived from our analysis are mostly smaller to values derived for SNR 443, except for CH_3OH , and (2) the molecules in the shocked gas of W 28 are less abundant than in the non-shocked gas of TMC-1, except SiO and CH_3OH . The abundances in IC 443 were determined using the same CO/ H_2 ratio of 10^{-4} whereas the abundances in TMC-1 were calculated with respect to an H_2 column density, of 10^{22} cm^{-2} that was assumed to be constant. Naturally, the comparison of abundances between W28

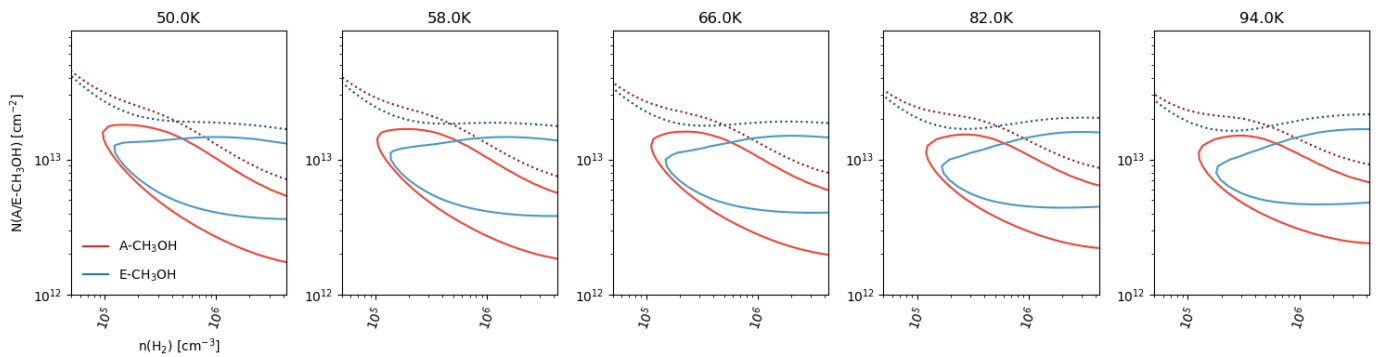


Fig. 10. 2D constant T_{kin} slices from a 3 dimensional grid of $\bar{\sigma}^2$. Contours of constant $\bar{\sigma}^2 = 9$ (solid); 25 (dotted) on a column density vs. H_2 density grid for detected lines of A- CH_3OH (red contours) and E- CH_3OH (blue contours) are shown.

F and IC 443 is more straightforward than the one between W28 F and TMC-1. We note that both $^{12}\text{CO}/[\text{H}_2]$ and $\text{N}[\text{H}_2]$ contribute to the uncertainties of the abundance calculations.

5.2. Physical properties in comparison with previous works

[Frail & Mitchell \(1998\)](#) observed three H_2CO transitions $3_{03}-2_{02}$, $3_{22}-2_{21}$, and $5_{05}-4_{04}$ towards W28 F to determine both kinetic gas temperature and density. Using the methods prescribed by [Mangum & Wootten \(1993a\)](#), they used the intensity ratio $3_{03}-2_{02}/3_{22}-2_{21}$ of 3.25 to estimate the kinetic temperature $T_{\text{kin}} = 80 \pm 10$ K. From our data we get a value of 3.9(4) for the same ratio. Similarly, [Frail & Mitchell \(1998\)](#) also used the $3_{03}-2_{02}/5_{05}-4_{04}$ ratio to determine the density, interpolating between the LVG models of [Mangum & Wootten \(1993a\)](#) using the kinetic temperature of 80 K to obtain $n_{\text{H}_2} = 2 \times 10^6 \text{ cm}^{-3}$. Our results obtained from the non-LTE RADEX model are consistent with their results.

An early theoretical work by [Elitzur \(1976\)](#) showed that collisions of OH with H_2 can create a strong inversion of the 1720 MHz line for a range of kinetic temperatures ($25 \leq T_{\text{kin}} \leq 200$ K) and molecular gas densities ($10^3 \leq n_{\text{H}_2} \leq 10^5 \text{ cm}^{-3}$) that are typical of the conditions expected in cooling post shock clouds. [Pavlakis & Kylafis \(1996a,b\)](#), and [Lockett et al. \(1999\)](#) included the effects of far-infrared line overlap (due to thermal and turbulent motions), and used newly computed collisional cross sections between OH and H_2 to confirm the basic result of [Elitzur \(1976\)](#) for a limited range of $T_{\text{kin}} = 50-125$ K. Given the higher critical densities of the probed methanol lines, our observations probe material that has a higher density than what would generally be conducive to the OH 1720 MHz line's inversion. We note that, in addition, the detected 36 GHz CH_3OH emission ([Pihlström et al. 2014](#)) as well as the thermal intensity peak of methanol in our observations are at a slight offset from the observed 1720 MHz position. In addition, the OH maser and the submillimeter lines observed could have different distributions along the line of sight and probe different volumes for this reason.

Studies of IC 443G in [van Dishoeck et al. \(1993\)](#) suggested that there is low density component, with $n_{\text{H}_2} \sim 10^5 \text{ cm}^{-3}$ and $T_{\text{kin}} \sim 80$ K, and a high density component, with $n_{\text{H}_2} \sim 3 \times 10^6 \text{ cm}^{-3}$, at a temperature of ~ 200 K. In our work, our lack of data for a sufficient number of higher energy H_2CO lines did not allow constraints on a two component gas. The results we obtain for W28 F indicate an emission region that has attributes from both of the IC 443 G components, with the kinetic tempera-

ture in W28 F being similar to that of the low density component in IC 443 G, while the spatial density of the former is similar to the high density component of the latter.

5.3. Ortho-para ratio of formaldehyde

In Sect. 4.1 we found similar spatial densities from ortho- and para- H_2CO line ratios. Therefore, assuming a spatial density of $n(\text{H}_2) = 2_{-1}^{+4} \times 10^6 \text{ cm}^{-3}$ (see Fig. 9), we could use Fig. 7 to constrain the ortho-para ratio. This was done by aligning the 3σ contours in Fig. 7. The resulting range for the ortho-para ratio is $1.5 \lesssim o/p \lesssim 3$.

For a full discussion of how the ortho to para ratio of formaldehyde is affected by different formation mechanisms, refer to [Kahane et al. \(1984\)](#) and references therein. Here we try to give a brief overview of the major factors that influence this ratio. In the gas phase, H_2CO is formed mostly via a reaction of CH_3^+ with O, but electronic recombination of H_3CO^+ may also make a contribution. Hence, the ortho/para ratio of H_2CO depends on the ortho/para ratio of these precursors. The interconversion between ortho- and para- H_2CO can also affect their ortho/para ratio. But, as [Kahane et al. \(1984\)](#) pointed out, the lifetime of H_2CO , which is determined by destruction by molecular ions is shorter than the time required for the ortho/para interconversion. If only gas-phase processes are important for H_2CO formation, irrespective of whether CH_3^+ or H_3CO^+ is the dominant precursor, [Kahane et al. \(1984\)](#) showed that the ortho/para ratio for formaldehyde should be $\sim 3-5$ at 10 K and ~ 3 at 70 K. However, atoms and molecules can get adsorbed onto grains and form H_2CO on their surface where their ortho/para ratio is likely to be thermalized at the grain temperature (i.e. the ratio corresponds to the Boltzmann distribution of ortho and para levels). Alternatively, H_2CO formed in the gas phase can get frozen out on the surface of grains and undergo ortho to para conversion if the grains contain paramagnetic species or magnetic nuclei, thereby lowering their ortho-para ratio ([Dickens & Irvine 1999](#)). An ortho/para ratio < 3 , which we find for W28 F, is therefore indicative of grain processing; i.e., either H_2CO was formed on grain surfaces followed by desorption from their surface, or, was adsorbed on grain surfaces after gas phase formation, processed there and then released back into a gas phase. Multiple mechanisms may be responsible for desorption of formaldehyde from grain surfaces, for example, thermal evaporation following Boltzmann's law, sporadic heating by cosmic rays ([Hasegawa & Herbst 1993](#)), photodissociation by external radiation field, and

via exothermic surface reactions (Duley & Williams 1993; Garrod et al. 2007).

Mangum & Wootten (1993b) studied multiple (ortho and para) H₂CO in a sample of star forming regions and use their data to determine kinetic temperatures and ortho-para ratios. Generally, they found relatively high values for the temperatures $> 70\text{K}$ and typical ortho-para ratios less than 3. In line with our findings, they concluded that “dust grains play an important role in H₂CO chemistry.”

6. Conclusions

We carried out a multi-molecular sub-millimeter wavelength line survey of the interaction zone of a molecular cloud with the supernova remnant W28. The APEX 12 m telescope was used to observe one of the locations (F) of the 1720 MHz OH maser emissions in a number of frequency ranges of the 230 and 345 GHz atmospheric windows. Emission from multiple molecular species, among which H₂CO, CH₃OH, SO, SiO, CS, HCO⁺ were detected. The lines’ centroid velocities and widths indicate that they all are originating from the same gas at $V_{\text{LSR}} \sim 7\text{ km s}^{-1}$ and $\Delta V \sim 10\text{ km s}^{-1}$. Non-LTE radiative transfer modeling of the lines with RADEX was used to determine the physical conditions of the cloud. For species with multiple line this modeling resulted in determinations of the kinetic temperature and H₂ density: formaldehyde lines were used to determine the kinetic temperature ($T_{\text{kin}} = 50 - 80\text{ K}$) and densities ($n(\text{H}_2) = 1 - 5 \times 10^6\text{ cm}^{-3}$). For the same reason, methanol line ratios from the same observing windows were used to constrain the H₂ density of the emitting cloud ($n(\text{H}_2) = 2^{+3}_{-1} \times 10^6\text{ cm}^{-3}$). We constrained the ortho-to-para ratio of formaldehyde to the range of $1.5 \lesssim o/p \lesssim 3$. This indicates formation of formaldehyde was most likely formed on the surface of dust grains instead of the gaseous phase. Absolute line intensities were modeled using RADEX to constrain the column densities of the emitting species by adopting the previously derived values for kinetic temperature and H₂ density. Using literature values for the CO column density, we were then able to put constraints on the abundances of various molecules.

Acknowledgements. We are indebted to the anonymous referee for invaluable input and many suggestions that resulted in a very significant improvement of this paper. We thank the staff of the APEX telescope for their assistance in observations. This work acknowledges support by The Collaborative Research Council 956, subproject A6, funded by the Deutsche Forschungsgemeinschaft (DFG). X.T. acknowledges support by The Heaven Lake Hundred-Talent Program of Xinjiang Uygur Autonomous Region of China and The National Natural Science Foundation of China under grant 11903070 and 11433008. This research has used NASA’s Astrophysical Data System (ADS).

References

Abdo, A. A., Ackermann, M., Ajello, M., et al. 2010, ApJ, 718, 348

Aharonian, F., Akhperjanian, A. G., Bazer-Bachi, A. R., et al. 2008, A&A, 481, 401

Anderl, S., Gusdorf, A., & Güsten, R. 2014, A&A, 569, A81

Ao, Y., Henkel, C., Menten, K. M., et al. 2013, A&A, 550, A135

Arikawa, Y., Tatematsu, K., Sekimoto, Y., & Takahashi, T. 1999, Publ. Astron. Soc. Jpn., 51, L7

Bolatto, A. D., Wolfire, M., & Leroy, A. K. 2013, ARA&A, 51, 207

Chevalier, R. A. 1999, ApJ, 511, 798

Claussen, M. J., Frail, D. A., Goss, W. M., & Gaume, R. A. 1997, ApJ, 489, 143

Dell’Ova, P., Gusdorf, A., Gerin, M., et al. 2020, A&A, 644, A64

Denoyer, L. K. 1979a, ApJL, 232, L165

Denoyer, L. K. 1979b, ApJL, 228, L41

Denoyer, L. K. 1983, ApJ, 264, 141

Dickens, J. E. & Irvine, W. M. 1999, ApJ, 518, 733

Dubner, G. M., Velázquez, P. F., Goss, W. M., & Holdaway, M. A. 2000, AJ, 120, 1933

Duley, W. W. & Williams, D. A. 1993, MNRAS, 260, 37

Dumas, G., Vaupré, S., Ceccarelli, C., et al. 2014, ApJ, 786, L24

Elitzur, M. 1976, ApJ, 203, 124

Frail, D. A., Kulkarni, S. R., & Vasisht, G. 1993, Nature, 365, 136

Frail, D. A. & Mitchell, G. F. 1998, ApJ, 508, 690

Fukui, Y. 2008, in American Institute of Physics Conference Series, Vol. 1085, American Institute of Physics Conference Series, ed. F. A. Aharonian, W. Hofmann, & F. Rieger, 104–111

Fukui, Y. & Tatematsu, K. 1988, in IAU Colloq. 101: Supernova Remnants and the Interstellar Medium, ed. R. S. Roger & T. L. Landecker, 261

Garrod, R. T., Wakelam, V., & Herbst, E. 2007, A&A, 467, 1103

Ginsburg, A., Darling, J., Battersby, C., Zeiger, B., & Bally, J. 2011, ApJ, 736, 149

Ginsburg, A., Henkel, C., Ao, Y., et al. 2016a, A&A, 586, A50

Ginsburg, A., Henkel, C., Ao, Y., et al. 2016b, A&A, 586, A50

Giuliani, A., Tavani, M., Bulgarelli, A., et al. 2010, A&A, 516, L11

Gratier, P., Majumdar, L., Ohishi, M., et al. 2016, ApJS, 225, 25

Green, A. J., Frail, D. A., Goss, W. M., & Otrupcek, R. 1997, AJ, 114, 2058

Green, D. A. 1998, VizieR Online Data Catalog, 7210

Gusdorf, A., Anderl, S., Güsten, R., et al. 2012, A&A, 542, L19

Gusdorf, A., Cabrit, S., Flower, D. R., & Pineau Des Forets, G. 2008, A&A, 482, 809

Hasegawa, T. I. & Herbst, E. 1993, MNRAS, 261, 83

Kahane, C., Lucas, R., Frerking, M. A., Langer, W. D., & Encrenaz, P. 1984, A&A, 137, 211

Koo, B.-C. & Moon, D.-S. 1997a, ApJ, 475, 194

Koo, B.-C. & Moon, D.-S. 1997b, ApJ, 485, 263

Leurini, S., Schilke, P., Menten, K. M., et al. 2004, A&A, 422, 573

Li, M., Bryan, G. L., & Ostriker, J. P. 2017, ApJ, 841, 101

Lockett, P., Gauthier, E., & Elitzur, M. 1999, ApJ, 511, 235

Mangum, J. G., Ginsburg, A. G., Henkel, C., et al. 2019, ApJ, 871, 170

Mangum, J. G. & Wootten, A. 1993a, ApJS, 89, 123

Mangum, J. G. & Wootten, A. 1993b, ApJS, 89, 123

Müller, H. S. P., Schlöder, F., Stutzki, J., & Winnewisser, G. 2005, Journal of Molecular Structure, 742, 215

Neufeld, D. A., Hollenbach, D. J., Kaufman, M. J., et al. 2007, ApJ, 664, 890

Ohishi, M., Irvine, W. M., & Kaifu, N. 1992, in Astrochemistry of Cosmic Phenomena, ed. P. D. Singh, Vol. 150, 171

Pavlakis, K. G. & Kylafis, N. D. 1996a, ApJ, 467, 300

Pavlakis, K. G. & Kylafis, N. D. 1996b, ApJ, 467, 309

Pickett, H. M., Poynter, R. L., Cohen, E. A., et al. 1998, JQSRT, 60, 883

Pihlström, Y. M., Sjouwerman, L. O., Frail, D. A., et al. 2014, AJ, 147, 73

Reach, W. T. & Rho, J. 1999, ApJ, 511, 836

Reach, W. T. & Rho, J. 2000, ApJ, 544, 843

Reach, W. T., Rho, J., & Jarrett, T. H. 2005a, ApJ, 618, 297

Reach, W. T., Rho, J., & Jarrett, T. H. 2005b, ApJ, 618, 297

Reach, W. T., Rho, J., Jarrett, T. H., & Lagage, P.-O. 2002, ApJ, 564, 302

Reach, W. T., Tram, L. N., Richter, M., Gusdorf, A., & DeWitt, C. 2019, ApJ, 884, 81

Rho, J. & Borkowski, K. J. 2002, ApJ, 575, 201

Rho, J., Jarrett, T. H., Tram, L. N., et al. 2021, arXiv e-prints, arXiv:2105.10617

Schilke, P., Walmsley, C. M., Pineau des Forets, G., & Flower, D. R. 1997, A&A, 321, 293

Schöier, F. L., van der Tak, F. F. S., van Dishoeck, E. F., & Black, J. H. 2005, A&A, 432, 369

Seta, M., Hasegawa, T., Dame, T. M., et al. 1998, ApJ, 505, 286

Seta, M., Hasegawa, T., Sakamoto, S., et al. 2004, AJ, 127, 1098

Sobolev, V. V. 1960, Moving envelopes of stars

Surdej, J. 1977, A&A, 60, 303

Tang, X. D., Henkel, C., Chen, C. H. R., et al. 2017a, A&A, 600, A16

Tang, X. D., Henkel, C., Menten, K. M., et al. 2018a, A&A, 609, A16

Tang, X. D., Henkel, C., Menten, K. M., et al. 2017b, A&A, 598, A30

Tang, X. D., Henkel, C., Wyrowski, F., et al. 2018b, A&A, 611, A6

Tatematsu, K., Fukui, Y., Iwata, T., Seward, F. D., & Nakano, M. 1990a, ApJ, 351, 157

Tatematsu, K., Fukui, Y., Landecker, T. L., & Roger, R. S. 1990b, A&A, 237, 189

Tatematsu, K., Fukui, Y., Nakano, M., et al. 1987, A&A, 184, 279

Tatematsu, K., Nakano, M., Yoshida, S., Wiramihardja, S. D., & Kogure, T. 1985, PASJ, 37, 345

Tielens, A. G. G. M. 2005, The Physics and Chemistry of the Interstellar Medium van der Tak, F. F. S., Black, J. H., Schöier, F. L., Jansen, D. J., & van Dishoeck, E. F. 2007, A&A, 468, 627

van Dishoeck, E. F., Jansen, D. J., & Phillips, T. G. 1993, A&A, 279, 541

Vassilev, V., Meledin, D., Lapkin, I., et al. 2008, A&A, 490, 1157

Velázquez, P. F., Dubner, G. M., Goss, W. M., & Green, A. J. 2002, AJ, 124, 2145

White, G. J. 1994, A&A, 283, L25

White, G. J., Rainey, R., Hayashi, S. S., & Kaifu, N. 1987, A&A, 173, 337

Wilner, D. J., Reynolds, S. P., & Moffett, D. A. 1998, AJ, 115, 247

Wootten, A. 1981, ApJ, 245, 105

Wootten, H. A. 1977, ApJ, 216, 440

Yuan, Y. & Neufeld, D. A. 2011, ApJ, 726, 76

Appendix A: Observed spectra towards W28 F

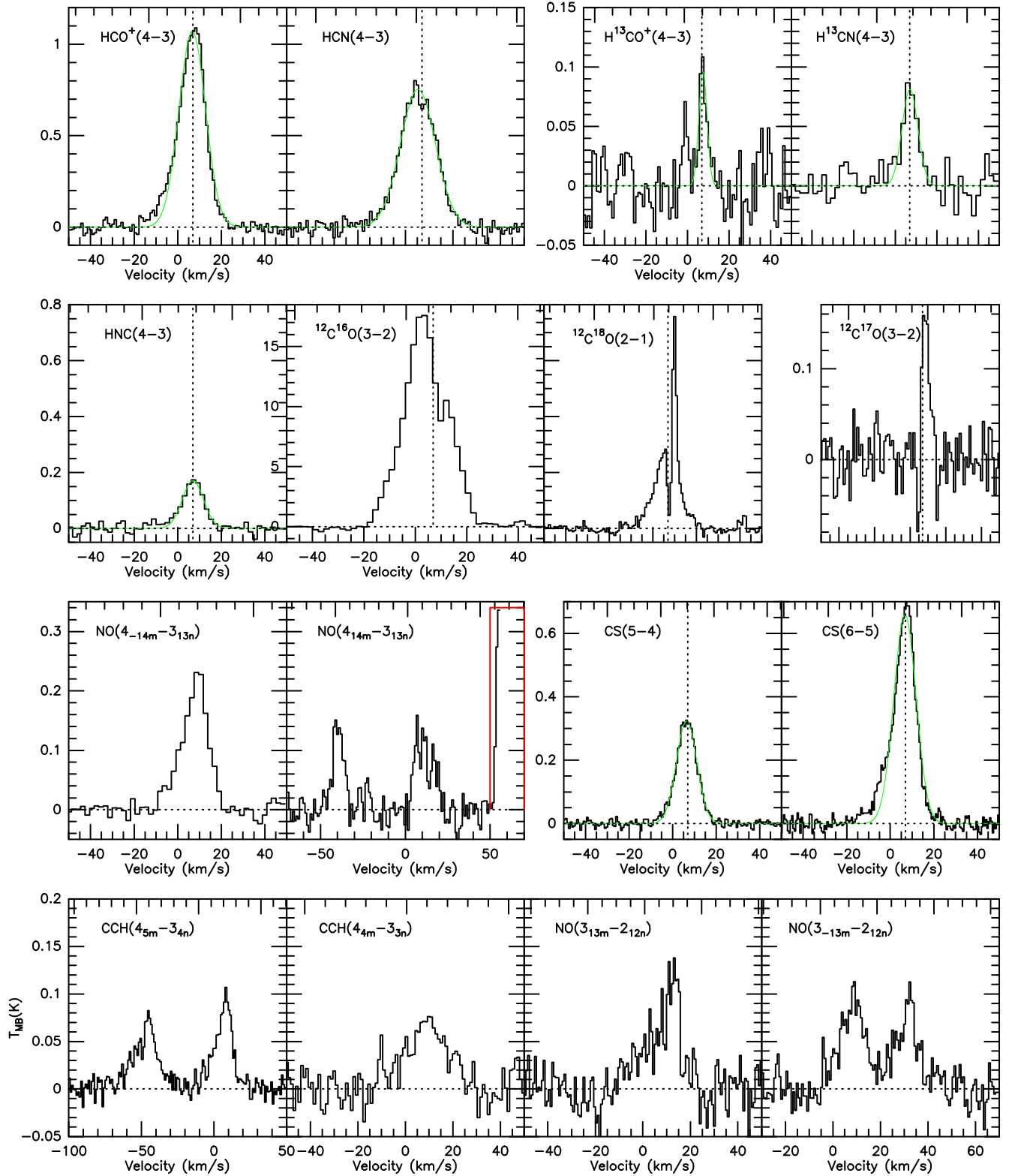


Fig. A.1. continued from Fig. 3. The spectral resolution lies between 0.8 km s^{-1} and 1.2 km s^{-1} .

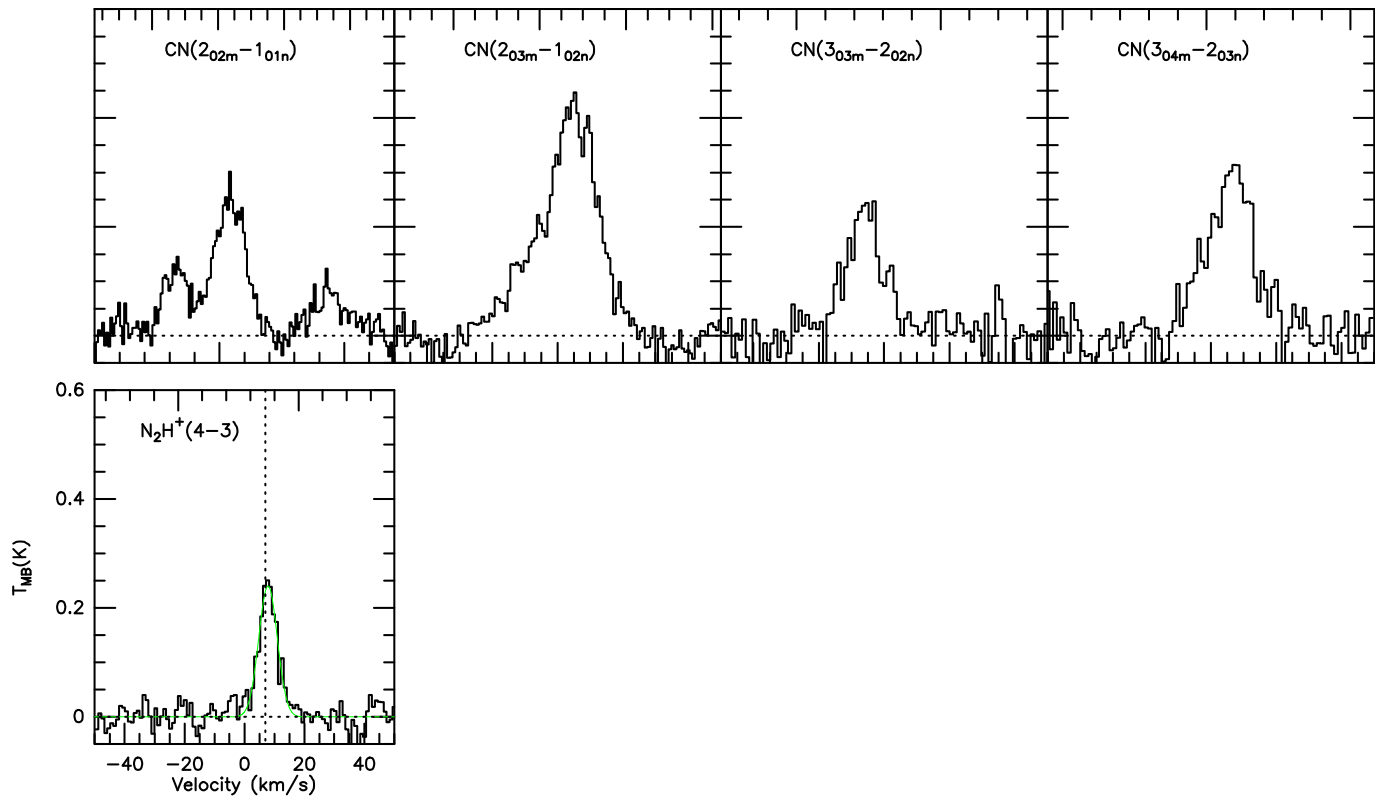


Fig. A.1. continued.

Appendix B: Parameters of observed spectra towards W28 F

Table B.1. Table. 2 continued.

Species	Transition	Frequency (MHz)	E_{up} (K)	$\int T_{\text{MB}} \text{d}v$ (K km s $^{-1}$)	V_{LSR} (km s $^{-1}$)	ΔV (km s $^{-1}$)	T_{MB} (K)
CN	$2_{0,2,1} - 1_{0,1,2}$	226616.571	16.3	-	-	-	$< 0.06^b$
	$2_{0,2,2} - 1_{0,1,2}$	226632.190	16.3	-	-	-	$< 0.11^d$
	$2_{0,2,3} - 1_{0,1,2}$	226659.558	16.3	-	-	-	$< 0.13^d$
	$2_{0,2,1} - 1_{0,1,1}$	226663.693	16.3	-	-	-	$< 0.13^d$
	$2_{0,2,2} - 1_{0,1,1}$	226679.311	16.3	-	-	-	$< 0.13^d$
	$2_{0,3,3} - 1_{0,2,2}$	226874.191	16.3	-	-	-	$< 0.14^d$
	$2_{0,3,4} - 1_{0,2,3}$	226874.781	16.3	-	-	-	$< 0.14^d$
	$2_{0,3,2} - 1_{0,2,1}$	226875.896	16.3	-	-	-	$< 0.14^d$
	$2_{0,3,2} - 1_{0,2,2}$	226887.420	16.3	-	-	-	$< 0.06^b$
	$2_{0,3,3} - 1_{0,2,3}$	226892.128	16.3	-	-	-	$< 0.06^b$
	$3_{0,3,3} - 2_{0,2,3}$	340008.126	32.6	-	-	-	$< 0.10^b$
	$3_{0,3,2} - 2_{0,2,2}$	340019.626	32.6	-	-	-	$< 0.10^b$
	$3_{0,3,4} - 2_{0,2,3}$	340031.549	32.6	-	-	-	0.07(2) ^a
	$3_{0,3,2} - 2_{0,2,1}$	340035.408	32.6	-	-	-	0.07(2) ^a
	$3_{0,3,3} - 2_{0,2,2}$	340035.408	32.6	-	-	-	0.07(2) ^a
	$3_{0,4,4} - 2_{0,3,3}$	340247.770	32.7	-	-	-	0.10(2) ^a
	$3_{0,4,5} - 2_{0,3,4}$	340247.770	32.7	-	-	-	0.10(2) ^a
	$3_{0,4,3} - 2_{0,3,2}$	340248.544	32.7	-	-	-	0.10(2) ^a
	$3_{0,4,3} - 2_{0,3,3}$	340261.773	32.7	-	-	-	$< 0.10^b$
	$3_{0,4,4} - 2_{0,3,4}$	340264.949	32.7	-	-	-	$< 0.10^b$
CCH	$4_{5,4} - 3_{4,4}$	349312.832	41.9	-	-	-	$< 0.03^b$
	$4_{5,5} - 3_{4,4}$	349337.706	41.9	0.68(7)	-	-	0.04(1) ^a
	$4_{5,4} - 3_{4,3}$	349338.988	41.9	0.68(7)	-	-	0.04(1) ^a
	$4_{4,4} - 3_{3,3}$	349399.276	41.9	0.66(7)	-	-	0.03(1) ^a
	$4_{4,3} - 3_{3,2}$	349400.671	41.9	0.66(7)	-	-	0.03(1) ^a
NO	$4_{4,3} - 3_{3,3}$	349414.643	41.9	-	-	-	$< 0.03^b$
	$3_{1,3,4} - 2_{-1,2,3}$	250436.848	19.2	-	-	-	$< 0.06^b$
	$3_{1,3,3} - 2_{-1,2,2}$	250440.659	19.2	-	-	-	$< 0.06^b$
	$3_{1,3,2} - 2_{-1,2,1}$	250448.530	19.2	-	-	-	$< 0.06^b$
	$3_{-1,3,4} - 2_{1,2,3}$	250796.436	19.3	-	-	-	$< 0.10^d$
	$3_{-1,3,3} - 2_{1,2,2}$	250815.594	19.3	-	-	-	$< 0.06^b$
	$3_{-1,3,2} - 2_{1,2,1}$	250816.954	19.3	-	-	-	$< 0.06^b$
	$4_{-1,4,5} - 3_{1,3,4}$	350689.494	36.1	-	-	-	0.05(1) ^{c,a}
	$4_{-1,4,4} - 3_{1,3,3}$	350690.766	36.1	-	-	-	0.05(1) ^{c,a}
	$4_{-1,4,3} - 3_{1,3,2}$	350694.772	36.1	-	-	-	0.05(1) ^{c,a}
	$4_{1,4,5} - 3_{-1,3,4}$	351043.524	36.1	-	-	-	0.05(1) ^a
	$4_{1,4,4} - 3_{-1,3,3}$	351051.705	36.1	-	-	-	0.05(1) ^a
	$4_{1,4,3} - 3_{-1,3,2}$	351051.705	36.1	-	-	-	0.05(1) ^a
CS	$5 - 4$	244935.557	35.3	3.57(5)	6.5(1)	11.0(2)	0.31(1)
	$6 - 5$	293912.086	49.4	8.34(8)	6.8(1)	11.6(1)	0.67(2)
HCO ⁺	$4 - 3$	356734.223	42.8	16.6(1)	6.6(1)	14.5(2)	1.07(3)
H ¹³ CO ⁺	$4 - 3$	346998.344	41.6	0.46(5)	7.8(3)	7(1)	0.06(1)
HCN	$4 - 3$	354505.477	42.5	14.4(3)	5.3(2)	17.8(4)	0.76(5)
H ¹³ CN	$4 - 3$	345339.769	41.4	0.74(10)	7.1(5)	8(1)	0.08(2)
HNC	$4 - 3$	362630.303	43.5	2.01(10)	7.0(3)	11.0(6)	0.17(2)
N ₂ H ⁺	$4 - 3$	372672.481	44.7	1.80(10)	7.9(2)	7.0(5)	0.24(3)
CO	$3 - 2$	345795.990	33.2	-	-	-	17.70(2) ^e
C ¹⁸ O	$2 - 1$	219560.354	15.8	-	-	-	0.59(1) ^e
C ¹⁷ O	$3 - 2$	337061.130	32.4	-	-	-	0.16(2) ^e

Notes. The T_{MB} values are the fit results and not the absolute peak observed values. In cases where no Gaussian fitting could be done, the observed temperature peaks have been shown.

(^a) These lines were blended with same E_{up} and A_{ij} values. They were fitted with one Gaussian and the integrated intensities were obtained by dividing the result of the fit by the number of blended lines assuming equal contribution from each. No attempt was made to derive LSR velocities or line widths.

(^b) 3 σ detection threshold applied for non-detected lines.

(^c) NO lines were blended with a CH₃OH line and hence only an estimate of the upper limit on the peak temperature could be established. For this, we assumed that the NO lines at \sim 351050 and \sim 350690 MHz have similar emission strengths because of their identical E_{up} and very similar A_{ij} values.

(^d) Multiple detected lines very closely spaced in frequency resulting a non-gaussian profile. No Gaussian fitting was done. Emission upper limits were determined from peak T_{MB} values.

(^e) CO line and its isotopes showed self absorption. Multiple Gaussian line fitting was not performed in this study. Hence, no Gaussian fitting was done to these lines.

Appendix C: Absolute intensity modeling with RADEX

All the integrated intensities were modeled on a 3D grid of kinetic temperature (T_{kin}), H₂ density ($n(\text{H}_2)$) and column density (N). Prior to modeling, the intensities were scaled to account for the differences in beamsize owing to different frequencies. A 20% uncertainty was added to the scaled intensities to account for the unknown beam-filling factor. The grid points were logarithmically distributed over the range of variables. A value of $\Delta V = 10 \text{ km s}^{-1}$ was used throughout. The background temperature was assumed to be that of the CMB, $T_{\text{CMB}} = 2.73 \text{ K}$. H₂ was considered as the only collision partner (see Sect. 4).

The output of RADEX was then compared to the observed intensities via an averaged sum of squared deviations at each grid point calculated by,

$$\bar{\sigma}^2 = \sum_i^{n_{\text{lines}}} \frac{(W_{\text{obs}_i} - W_{\text{mod}_i})^2}{\sigma_{W_{\text{obs}_i}}^2} \Big/ n_{\text{lines}}, \quad (\text{C.1})$$

where n_{lines} is equal to the total number of observed transitions. The contours of constant $\bar{\sigma}^2$ were then plotted on the density versus column density grid for a constant temperature. Also, $\bar{\sigma}^2 = 9$ stands for $\sim 99.7\%$, making it likely that the intensity observed is due to a grid point inside this contour. The $\bar{\sigma}^2 = 25$ contour means that $\sim 99.99\%$ likely that the intensity observed is due to a grid point inside this contour.

Appendix D: RADEX modeling results for other molecules

Calibration uncertainties were accounted for with a 20% error for each line intensity. Figure D.1 shows the projection of constant $\bar{\sigma}^2$ on the column density and spatial density plane for a given kinetic temperature.

Table C.1. RADEX grid.

T_{kin} vs. $n(\text{H}_2)$ ^a	
T_{kin} $n(\text{H}_2)$	30 - 150 K $10^5 - 10^7 \text{ cm}^{-3}$
N vs. $n(\text{H}_2)$	
$N [\text{cm}^{-2}]$	H_2CO
$n(\text{H}_2) [\text{cm}^{-3}]$	$10^{12} - 10^{14}$
$T_{\text{kin}} [\text{K}]$	$5 \times 10^4 - 5 \times 10^6$
$5 \times 10^4 - 5 \times 10^6$	$10^{13} - 10^{15}$
$50 - 100$	$5 \times 10^4 - 5 \times 10^6$
$50 - 100$	$7 \times 10^{12} - 10^{15}$
$50 - 100$	$5 \times 10^4 - 10^7$
$50 - 100$	$5 \times 10^{11} - 10^{14}$
$50 - 100$	$3 \times 10^{12} - 10^{15}$
$50 - 100$	$10^5 - 10^8$

Notes. ^(a) N is fixed but its effect are shown in the N vs $n(\text{H}_2)$.

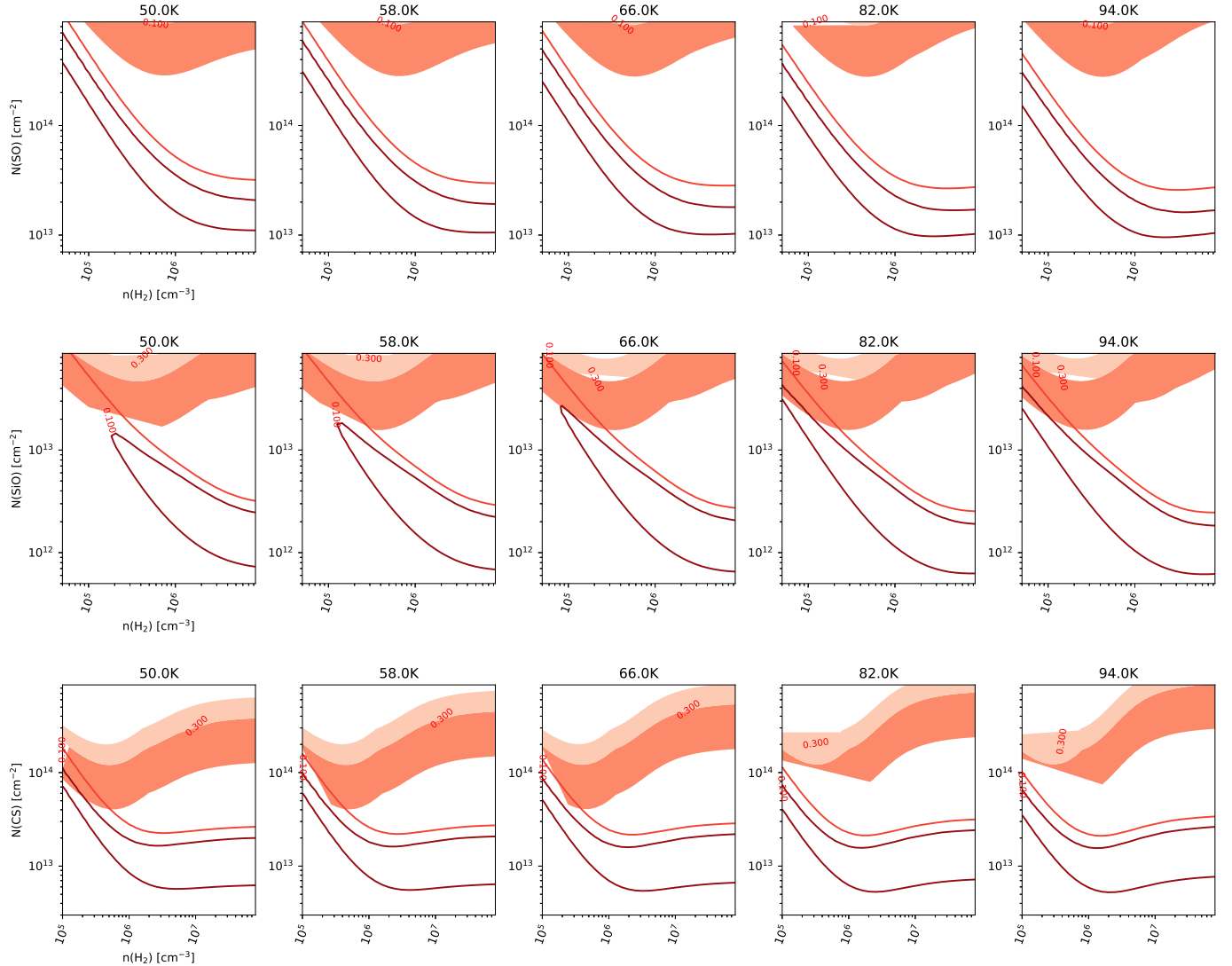


Fig. D.1. 2D constant T_{kin} slices from a 3 dimensional grid of $\bar{\sigma}^2$ for SO (top), SiO (middle) and CS (bottom). Contours of constant $\bar{\sigma}^2 = 9$ (darker); 25 (lighter) on a column density vs. H_2 density grid for detected lines are shown. The background shades show the optical depths $\tau = 0.05$ (darker region) and 0.1 (lighter region) for all species. These optical depths correspond to the maximum optical depth out of all the lines modeled.

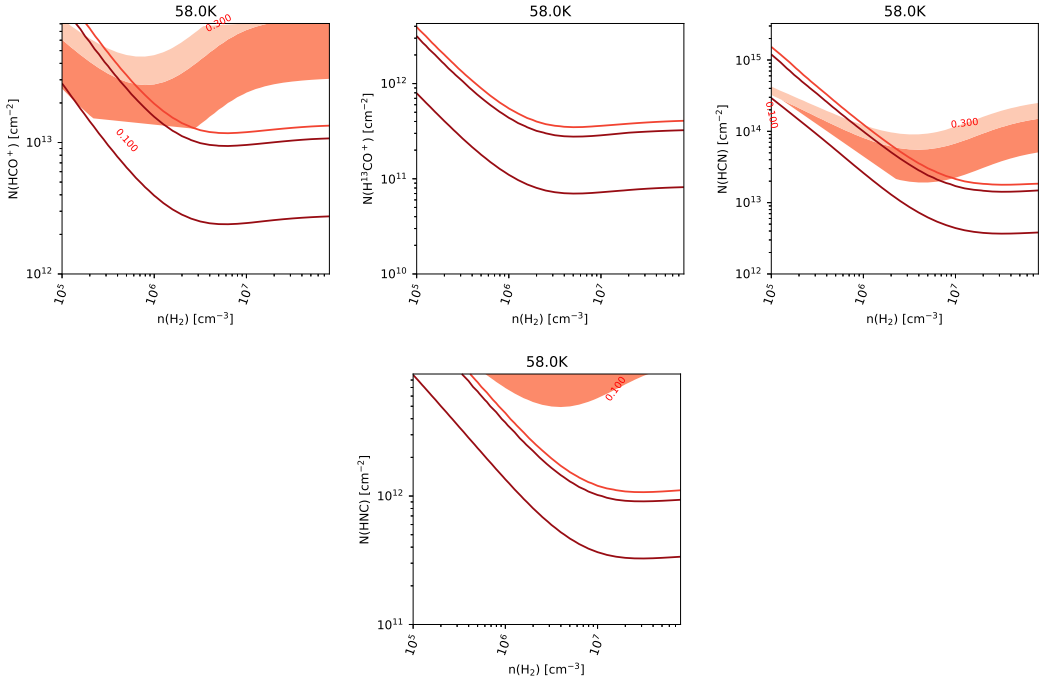


Fig. D.2. Results of modeling individual line intensities with RADEX on a 2D grid of column densities and spatial densities for a constant T_{kin} . Contours of constant $\bar{\sigma}^2 = 9$ (darker); 25 (lighter) for detected lines are shown. The background shades show the optical depths $\tau = 0.05$ (darker region) and 0.1 (lighter region) for the corresponding species.